

## A NEW REDUCTION OF THE BLANCO COSMOLOGY SURVEY: AN OPTICALLY SELECTED GALAXY CLUSTER CATALOG AND A PUBLIC RELEASE OF OPTICAL DATA PRODUCTS

L. E. BLEEM<sup>1,2</sup>, B. STALDER<sup>3</sup>, M. BRODWIN<sup>4</sup>, M. T. BUSHA<sup>5,6</sup>, M. D. GLADDERS<sup>2,7</sup>,  
F. W. HIGH<sup>2,7</sup>, A. REST<sup>8</sup>, AND R. H. WECHSLER<sup>5,6,9</sup>

<sup>1</sup> Argonne National Laboratory, 9700 South Cass Avenue, Argonne, IL 60439, USA

<sup>2</sup> Kavli Institute for Cosmological Physics, University of Chicago, 5640 South Ellis Avenue, Chicago, IL 60637, USA

<sup>3</sup> Harvard-Smithsonian Center for Astrophysics, 60 Garden Street, Cambridge, MA 02138, USA

<sup>4</sup> Department of Physics and Astronomy, University of Missouri, 5110 Rockhill Road, Kansas City, MO 64110, USA

<sup>5</sup> Kavli Institute for Particle Astrophysics and Cosmology 452 Lomita Mall, Stanford University, Stanford, CA 94305, USA

<sup>6</sup> SLAC National Accelerator Laboratory, 2575 Sand Hill Road, MS 29, Menlo Park, CA 94025, USA

<sup>7</sup> Department of Astronomy and Astrophysics, University of Chicago, 5640 South Ellis Avenue, Chicago, IL 60637, USA

<sup>8</sup> Space Telescope Science Institute, 3700 San Martin Drive, Baltimore, MD 21218, USA

<sup>9</sup> Department of Physics, Stanford University, Stanford, CA 94305, USA

Received 2014 April 2; accepted 2014 November 16; published 2015 January 19

### ABSTRACT

The Blanco Cosmology Survey is a four-band (*griz*) optical-imaging survey of  $\sim 80 \text{ deg}^2$  of the southern sky. The survey consists of two fields centered approximately at  $(\text{R.A.}, \text{decl.}) = (23^\text{h}, -55^\circ)$  and  $(5^\text{h}30^\text{m}, -53^\circ)$  with imaging sufficient for the detection of  $L_\star$  galaxies at redshift  $z \leq 1$ . In this paper, we present our reduction of the survey data and describe a new technique for the separation of stars and galaxies. We search the calibrated source catalogs for galaxy clusters at  $z \leq 0.75$  by identifying spatial over-densities of red-sequence galaxies and report the coordinates, redshifts, and optical richnesses,  $\lambda$ , for 764 galaxy clusters at  $z \leq 0.75$ . This sample,  $>85\%$  of which are new discoveries, has a median redshift of  $z = 0.52$  and median richness  $\lambda(0.4 L_\star) = 16.4$ . Accompanying this paper we also release full survey data products including reduced images and calibrated source catalogs. These products are available at <http://data.rcc.uchicago.edu/dataset/blanco-cosmology-survey>.

**Key words:** galaxies: clusters: general – surveys – techniques: photometric

**Supporting material:** machine-readable tables

### 1. INTRODUCTION

Multi-band optical imaging surveys provide powerful data sets with which to study cosmology. Technological improvements over the past two decades have led to a rapid increase in the number of such surveys. Notable examples include the large-area Sloan Digital Sky Survey (SDSS; York et al. 2000), deeper, moderate-area surveys such as the Red Sequence Cluster Survey (Gladders & Yee 2005), and the Canada–France–Hawaii Telescope Legacy Survey,<sup>10</sup> and a new generation of both large ( $\gtrsim 1000 \text{ deg}^2$ ) and deep surveys including the Panoramic Survey Telescope & Rapid Response System (Kaiser et al. 2010), RCS2 (Gilbank et al. 2011), the Dark Energy Survey,<sup>11</sup> and the Subaru Hyper Suprime-Cam project (Takada 2010) highlight further advances in the field.

Such surveys are particularly useful for constraining cosmology with galaxy clusters as large areas are required to obtain statistically useful numbers of these rare, massive objects. The identification of galaxy clusters in optical survey data has a rich history beginning with Abell’s visual identification of over-densities of galaxies in the Palomar Sky Survey (Abell 1958) and continuing with modern approaches that identify clusters as significant spatial concentrations of the red, passively evolving E/S0 galaxies that form the red-sequence in clusters (e.g., Gladders & Yee 2000; Koester et al. 2007a; Hao et al. 2010; Rykoff et al. 2014) or of galaxies in photometric redshift space (e.g., Wen et al. 2009, 2012; Szabo et al. 2011; see Allen et al. 2011 for a recent review).

With the maturation of cluster-identification techniques, the critical challenge remaining for cosmology with optically-selected cluster samples is connecting observable cluster properties (often quantified as a “richness” parameter related to the number of galaxies in the cluster) to the mass of the system. Here, weak-lensing and complimentary multi-wavelength data from X-ray and millimeter-(mm-)wave<sup>12</sup> surveys can both greatly improve cluster mass-calibration and provide powerful cross-checks by testing the self-consistency of proposed mass-richness scaling relations (e.g., Cunha 2009; Wu et al. 2010). Indeed, recent joint optical- and SZ-analyses of the maxBCG cluster sample (Koester et al. 2007a) with SZ data from the *Planck* satellite (Planck Collaboration et al. 2011) and the Atacama Cosmology Telescope (ACT; Sehgal et al. 2012) have revealed tensions between the assumed SZ-mass and optical richness–mass scaling relations and highlight the power of such multi-wavelength studies to test the robustness of observable-mass scaling relations (Rozo et al. 2012).

The optical *griz*-band Blanco Cosmology Survey (BCS; Menanteau et al. 2009, 2010; Desai et al. 2012) while of modest ( $\sim 80 \text{ deg}^2$ ) size and depth, is particularly interesting owing to the wealth of multi-wavelength data in the survey region. In addition to being within the footprint of both the  $2500 \text{ deg}^2$  South Pole Telescope SZ Survey (SPT; Carlstrom et al. 2011) and the ACT mm-wave survey (Dünner et al. 2013), one of the two BCS fields contains the XMM-BCS survey (Šuhada et al. 2012), a subset of a new *XMM* survey, the XXL,<sup>13</sup> and

<sup>10</sup> <http://www.cfht.hawaii.edu/Science/CFHLS/>  
<sup>11</sup> [www.darkenergysurvey.org](http://darkenergysurvey.org)

<sup>12</sup> Where clusters have imprinted their signature via the Sunyaev–Zel’dovich (SZ) effect (Sunyaev & Zel’dovich 1972).

<sup>13</sup> <http://irfu.cea.fr/xxl/>

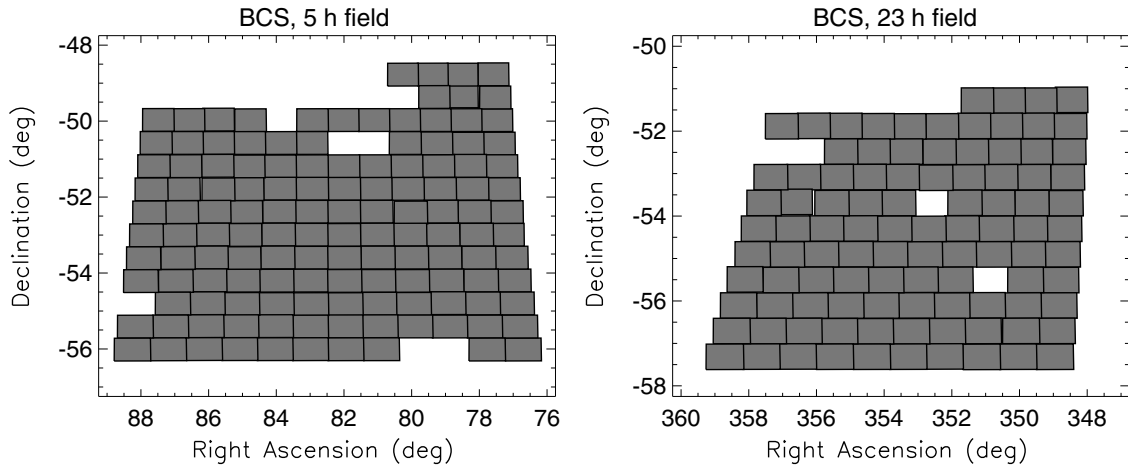


**Figure 1.** Spatial footprint of the imaging data presented in this work. Coadded images and inverse-noise weight maps for each tile are available in the  $g$ ,  $r$ ,  $i$ , and  $z$  bands.

is itself contained within the  $100 \text{ deg}^2$  SPT Deep Field which features mm-wave data from SPTpol (Austermann et al. 2012), near-infrared imaging from *Spitzer* (Ashby et al. 2013) and 250, 350 and  $500 \mu\text{m}$  imaging from *Herschel*/SPIRE (Holder et al. 2013).

In this paper, we present our reduction of imaging data from the BCS. As first step toward a broader multi-wavelength study of clusters in the survey region, we also identify galaxy clusters in these calibrated data. This work is presented as follows: in Section 2.2, we provide a brief overview of the BCS and describe our image reduction pipeline and photometric calibration. We describe the galaxy cluster detection algorithm in Section 3, and our characterization of the detected clusters in Section 4. In Section 5, we discuss tests of our cluster-finding algorithm on simulated catalogs and in Section 6 compare our results to previous cluster catalogs that overlap the BCS region. Finally, we conclude in Section 7. Where applicable we assume a flat  $\Lambda\text{CDM}$  cosmology with  $\Omega_M = 0.27$  and  $h = 0.71$ . Unless otherwise specified, all masses are reported in terms of  $M_{200}$ , where  $M_{200}$  is defined as the mass contained within a radius  $r_{200}$  at which the average density is 200 times the critical density, and all magnitudes are reported in the AB system.

## 2. DATA OVERVIEW AND REDUCTION

In this section we provide a brief overview of the Blanco Cosmology Survey. We describe our production of calibrated images and source catalogs from the publicly available imaging data as well as our application of a new star–galaxy separation algorithm to these data.

### 2.1. Survey Overview

The BCS, an National Optical Astronomy Observatory (NOAO) large survey program (2005B-0043), is a four-band ( $griz$ ) optical-imaging survey that covers  $\sim 80 \text{ deg}^2$  of the southern sky. The survey was designed to reach depths sufficient to detect  $L_*$  galaxies out to a redshift of  $z = 1$  in the  $i$ - and  $z$ -band data (Desai et al. 2012). The data presented here were acquired during 57 nights split over six observing runs between 2005 November and 2008 November using the MOSAIC II imager<sup>14</sup> on the 4 m Blanco Telescope at Cerro Tololo Inter-American Observatory, Chile. The MOSAIC II camera is composed of

eight  $2k \times 4k$  SITE charge-coupled devices (CCDs) with a plate scale of  $0''.27$  per pixel, resulting in a  $36' \times 36'$  field of view. The camera was operated in 16 channel mode (in which each CCD is read out with two amplifiers) throughout the survey.

The survey consists of two fields roughly centered at (R.A., decl.) =  $(23^\text{h}, -55^\circ)$  and  $(5^\text{h}30^\text{m}, -53^\circ)$ . The two survey fields were observed in small “tiles” roughly the size of the MOSAIC II field of view. Here we present reductions of 133 tiles for the 5 h field and 100 tiles for the 23 h field covering  $\sim 45 \text{ deg}^2$  and  $\sim 33 \text{ deg}^2$ , respectively<sup>15</sup>; the footprint of the reduced tiles is shown in Figure 1. Each individual tile nominally consists of  $2 \times 125$  s,  $2 \times 300$  s,  $3 \times 450$  s, and  $3 \times 235$  s exposures in the  $g$ ,  $r$ ,  $i$ , and  $z$  bands, respectively, though the actual number of exposures can vary owing to variable observing conditions over the course of the survey. Exposures are offset several arc minutes to cover chip gaps and to provide overlap between neighboring tiles. For further details on the survey motivations and observational strategy readers are referred to previous publications (Menanteau et al. 2009, 2010; Desai et al. 2012).

### 2.2. Image Reduction

The imaging data is reduced with the PHOTPIPE pipeline. This pipeline, initially developed for the SuperMACHO and ESSENCE projects is described in detail in Rest et al. (2005) and Miknaitis et al. (2007). For all images the reduction process includes masking of bad and saturated pixels, crosstalk correction, overscan correction, debiasing, flat fielding, and illumination corrections. Illumination corrections for each band are determined on a nightly basis using a master flat created by combining all of the science exposures in a given band. For nights/bands with insufficient numbers of exposures (we find a minimum of 11 images without bright stars is necessary to create good master flat) we apply corrections from nearby nights. The  $i$ - and  $z$ -band images are also corrected for fringing. Fringe patterns on images from the MOSAIC II camera are quite stable and we obtain good results using fringe frames constructed from all science exposures obtained in a given band during an observing run.

Next, in preparation for coadding the images, an initial source finding run is performed on the single epoch images using

<sup>14</sup> <http://www.ctio.noao.edu/content/MOSAIC-II-CCD-Imager>

<sup>15</sup> We have adopted the original field names in the NOAO archive for our tile naming scheme and note that our names can differ from Desai et al. (2012) for the same region of sky.

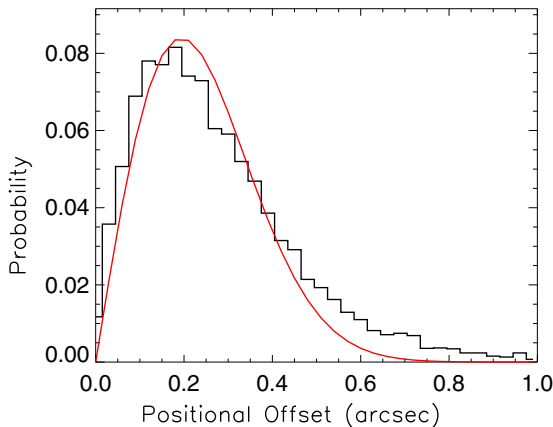


**Figure 2.** Astrometric residuals of BCS sources associated with 2MASS sources. Plotted are the residuals of sources with  $16 < J < 16.5$  (Vega) and  $J$ -band uncertainty  $\leqslant 0.25$ . Overplotted is the best-fit Gaussian model with  $0''.194$  positional uncertainty. We restrict the magnitude range of the 2MASS data plotted for clarity as the positional scatter is a strong function of magnitude (signal to noise) at the faint end of the 2MASS catalog.

SExtractor (Bertin & Arnouts 1996) v2.8.6 to both determine the astrometric calibration and the relative zeropoints of all images for each band in a tile. The astrometric calibration is tied to the Two Micron All Sky Survey (2MASS) catalog (Skrutskie et al. 2006) and the astrometric solution shows residuals of  $\sim 0''.2$  (see Figure 2). These residuals are roughly equal to the positional uncertainty of the typical 2MASS sources ( $J$ -band  $\sim 16.3$  Vega) that are associated with the BCS sources.

Following the determination of relative zeropoints using high signal-to-noise sources found in common in multiple images of a tile, the individual tile images are reprojected to a common center with a pixel scale of  $0''.3$  per pixel and coadded using SWarp (Bertin et al. 2002). Inverse noise-variance maps used as weight maps during final source detection are also generated at this stage. The distribution of seeing—computed as the average FWHM of the seeing disk in the single epoch images that compose the coadd—for each of the BCS tiles as well as the  $5\sigma$  point source depths for the coadded images are shown in Figure 3. The median values of the seeing in the  $g$ ,  $r$ ,  $i$ ,  $z$  bands are [ $1''.13$ ,  $1''.05$ ,  $0''.97$ ,  $0''.99$ ] and the median  $5\sigma$  point source magnitudes are [24.2, 24, 23.5, 22.2], respectively. The seeing distributions are not symmetric but are highly skewed toward poorer seeing.

After coaddition, the tiles are visually inspected and areas with significant artifacts (predominately corresponding to halos around the very brightest stars or noisy amplifiers) are identified and weight maps in these areas are set to zero. As the centers of tiles in the different filters are sometimes slightly offset, the coadded images are then slightly trimmed to  $36'' \times 36''$  to help ensure sky coverage in all four bands. For  $\sim 1 \text{ deg}^2$  of survey data (distributed over many tiles) we have excluded  $g$ -band data owing to excess noise on the CCDs. Finally, as discussed below, we create flag images for use in the source extraction step based on the weight maps; we flag regions with weight less than 10% of the maximum weight.

### 2.3. Source Extraction and Flagging

Sources are extracted from the coadded images by running SExtractor in dual image mode using the  $i$ -band images for detection and extracting  $griz$  MAG\_AUTO and  $4''$  aperture

**Table 1**  
SExtractor Source Detection Settings

DETECT_TYPE	CCD
DETECT_MINAREA	$1.1\pi \times (i\text{-band seeing})^2$
THRESH_TYPE	RELATIVE
DETECT_THRESH	1.2
ANALYSIS_THRESH	1.2
FILTER	Y
FILTER_NAME	default.conv
DEBLEND_NTHRESH	32
DEBLEND_MINCONT	0.005
BACKPHOTO_TYPE	LOCAL

**Notes.** SExtractor settings used in the extraction of source catalogs. SExtractor was run in dual image mode with the  $i$ -band images set as the detection images. The  $i$ -band seeing value refers to the average FWHM of the seeing disk in the single epoch images that compose the coadds.

magnitudes at the locations of detected sources. Detection settings are provided in Table 1.

We apply a correction to the magnitude uncertainties returned by SExtractor as we find these values underestimate the true scatter in the data. The correction is estimated by measuring the sky noise—the dominant contribution to the flux uncertainty for faint sources—in the coadded images utilizing a modified version of the Monte-Carlo based technique described in Ashby et al. (2009). In brief, we estimate the sky noise by performing photometry with  $4''$  apertures at 1500 random positions in the central region of each coadded image. We then fit a Gaussian function to the resulting flux distribution, excluding the bright tail which is biased by real sources in the image. We compare the measured scatter to the median  $4''$  aperture flux uncertainty estimated by SExtractor for sources from this same region and estimate our correction factor as the ratio between the two; the corrected uncertainties are typically  $1.3$  to  $1.5 \times$  greater than the initial values estimated by SExtractor. We have verified this correction by comparing the distribution of differences in magnitudes for objects measured in sequential exposures (obtained under essentially identical observing conditions) with the corrected magnitude uncertainties and find good agreement. The amplitude of our correction also agrees with that determined in Brown et al. (2007) who found a 40% underestimate in the MAG\_AUTO magnitude uncertainties. This method works for sources with signal to noise  $\gtrsim 2.5$ , below which there is again extra scatter not reflected by the rescaled error bars. The  $5\sigma$  point source depths plotted in Figure 3 are derived from corrected uncertainties on point sources. We find for the detection band,  $i$  band, these depths correspond to the peaks in number counts distributions.

We next identify and flag sources that may have biased flux measurements owing to their proximity to bright stars. Such stars are often surrounded by “halo-like” features in the image caused by internal reflections in the camera. We find it necessary to flag regions around stars brighter than 14 (Vega) in the  $J$  band; at fainter magnitudes default flagging from the weight maps is sufficient. All stars with  $J$ -band magnitude brighter than 7 (Vega) are visually inspected in pseudo-rgb color images generated from the  $z$ -,  $i$ -,  $r$ -band coadded images and the affected regions are flagged. Fifty stars in the 23 h field and 101 stars in the 5 h field are brighter than this magnitude cut. For the fainter stars, flagged regions were automatically generated in circular apertures around each star. The radii of these apertures were

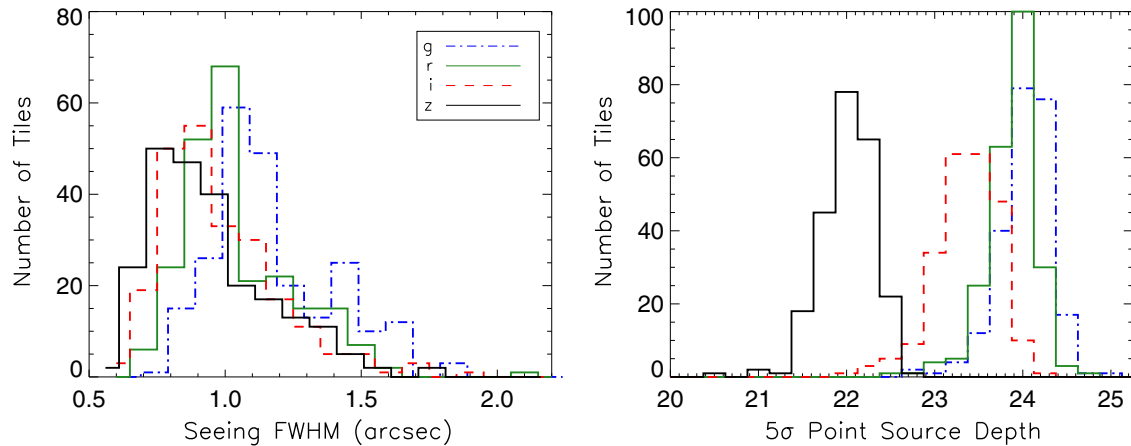


**Figure 3.** Seeing distribution and  $5\sigma$  corrected MAG\_AUTO point source depths for the 233 tiles presented in this work. The plotting scheme is the same in both panels: the  $g$  band is traced by blue dot-dash, the  $r$  band is solid green, the  $i$  band is dashed red, and the  $z$  band is solid black. In the left panel, the  $g$ - and  $z$ -band distributions are offset slightly to the right and left, respectively, for clarity. The median values of the seeing in the  $g$ ,  $r$ ,  $i$ ,  $z$  bands are [ $1''.13$ ,  $1''.05$ ,  $0''.97$ ,  $0''.99$ ] and the median  $5\sigma$  point source magnitudes are [24.2, 24, 23.5, 22.2], respectively.

conservatively chosen based on inspection of a subset of stars. The aperture radii ranged from  $2'$  at  $J = 7$  (Vega) to  $0'.25$  at  $J = 14$  (Vega). Sources in these flagged regions are excluded when fitting for the photometric calibration parameters for each tile (described below), but are retained in the released catalogs and flagged as having potentially biased photometry.

Finally, we flag sources based on their location in the tile. As described above, the BCS tiles are nominally composed of two or three exposures in each filter, with offsets of several arc minutes between exposures. As we are processing the survey on a tile-by-tile basis (as opposed to coadding all images of a given filter into a single monolithic block for each survey field) this naturally leads to shallower regions at the edges of the tiles. To facilitate analyses which require more even coverage, we mark each source as coming from the central (i.e., uniform coverage) or edge region of each tile.

#### 2.4. Photometric Calibration

We calibrate the colors and absolute magnitudes of stars and galaxies using Stellar Locus Regression (SLR; High et al. 2009). SLR calibrates colors by matching the instrumental colors of stars to that of a universal stellar color–color locus as measured by  $\sim 10^5$  stars in the SDSS (Covey et al. 2007). Absolute calibration with SLR proceeds analogously to other color–color calibrations but with one of the colors constructed from an instrumental magnitude combined with a calibrated magnitude from an overlapping survey. SLR has previously been used to calibrate the photometry for pointed follow-up of SPT-detected galaxy clusters (e.g., High et al. 2010; Song et al. 2012), an alternate reduction of the BCS (Desai et al. 2012), and similar techniques have been utilized elsewhere in the literature for the photometric calibration of large surveys (Gilbank et al. 2011) and to compliment more standard calibration (Ivezić et al. 2007). As discussed in High et al. (2009), SLR naturally corrects for atmospheric and—as the majority of the stars at BCS survey depths are behind the Galactic dust sheet—Galactic extinction.

For each tile, we identify stars for photometric calibration by selecting sources with signal to noise  $\geq 3$  in the color combinations of interest, SExtractor CLASS\_STAR  $\geq 0.95$  in the  $r$  and  $i$  bands and require the source to be located in the central region of the tile. By using only the central portion of the coadd to determine the photometric calibration, we can use the

**Table 2**  
Color Terms

Filter	Color Term	Color Multiplier
$g$	$-0.1344$	$g - r$
$r$	$-0.0103$	$r - i$
$i$	$-0.1148$	$r - i$
$z$	$0.0028$	$r - z$

**Note.** Color terms and color multipliers applied in the calibration of source catalogs from the BCS.

overlapping regions at the edges of the tiles as an independent check of our calibration.

We next perform the stellar locus regression and transform the native MOSAIC II magnitudes to the SDSS system using a single set of color terms for all CCDs (Table 2). The color terms were measured by performing a first order fit between MOSAIC II instrumental and SDSS magnitudes in several SDSS-observed star fields. When correcting for extinction and color terms, it is necessary to chose a color multiplier in the transformation from raw to calibrated colors. In general, broad filter combinations (such as  $g - i$ ) are beneficial as they provide wide leverage over the range of stellar colors. However, owing to the relatively shallow depth in the  $g$  band of the BCS catalogs with respect to high-redshift  $L_*$  galaxies (and as these catalogs were constructed for detection of red-sequence cluster galaxies), we chose the color multiplier to always include the  $r$ -band filter.

The absolute flux scaling is calibrated using SLR by matching bright stars in the BCS with stars from the 2MASS point source catalog (Skrutskie et al. 2006). Determining robust zeropoints proved to be the most difficult part of the calibration process, so we discuss the process in some detail here.

The quality of the zeropoints can be assessed by obtaining zeropoints for each of the filters and comparing colors constructed by differencing these absolute magnitudes against colors from the SLR-color calibration. Initial calibration (without the flagging generated from the weight maps introduced in Section 2.2) revealed large discrepancies between these two sets of calibrated colors. We found that these discrepancies were largest for tiles observed in the best conditions and also noticed that the brighter, bluer stars systematically deviated from the median locus relation—both of these symptoms pointed to saturated stars being included in the zeropoint calibration.

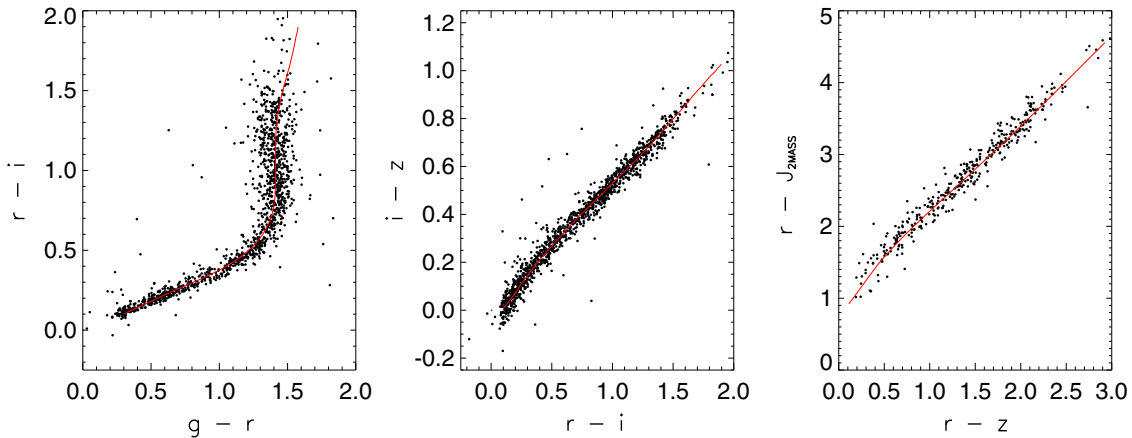


**Figure 4.** Color–color diagram of a subsample of stars with  $\text{SG} > 0.8$  (see Section 2.6) and color errors less than 0.25 mag after photometric calibration of BCS tile 0548–5524. Overplotted in red are the median color–color relations of the stellar locus as reported in Covey et al. (2007).

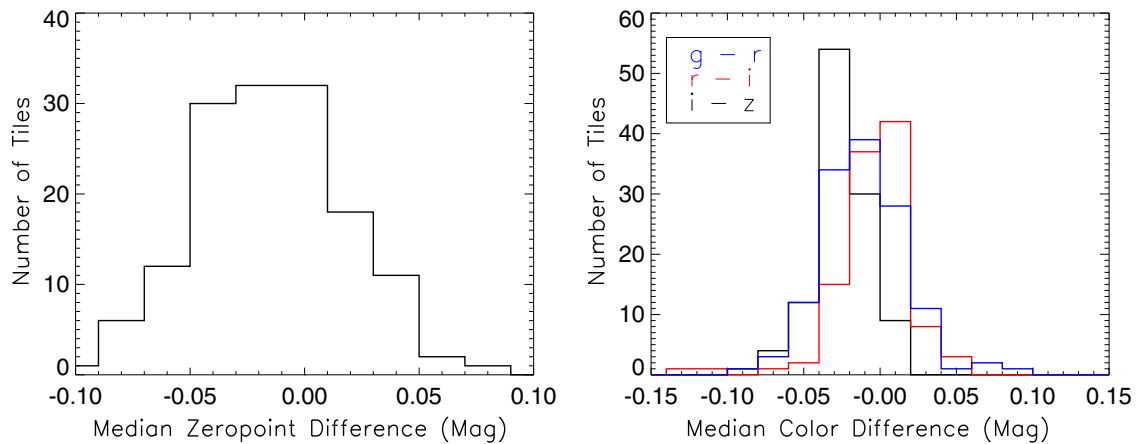


**Figure 5.** Median  $i$ -band magnitude (Left) and  $g - r$ ,  $r - i$ ,  $i - z$  color (Right) differences for objects that lie in the overlapping region between neighboring tiles. We report magnitude and color statistics for all tiles with  $\geq 100$  (75) sources with signal to noise  $\geq 4$  in the  $r$ ,  $i$ ,  $z$  ( $g$ ) bands corresponding to 204 (188) of the 233 survey tiles. We divide the standard deviation measured from these distributions by  $\sqrt{2}$  to obtain the uncertainty on the calibration for a single tile. We measure 2.4% rms variation in the  $i$ -band zeropoints and 1.9%, 1.3%, and 1.3% rms in the  $g - r$ ,  $r - i$ , and  $i - z$  calibration, respectively.

To solve this problem, we use the SWarp-generated weight maps to identify the non-masked saturated sources.<sup>16</sup> The algorithm that creates these weight maps includes a contribution from the Poisson error from bright sources,<sup>17</sup> which makes it possible to identify the locations of saturated sources in the map prior to source extraction. We find that flagging objects whose weight is less than 10% of the maximum weight is sufficient to exclude saturated objects. Owing to the long (450 s) exposures in the  $i$  band a number of tiles had too few non-saturated 2MASS sources in the  $i$ -band-selected catalogs to provide accurate calibration. We instead determine zeropoints for all tiles using the  $grz$ -band magnitudes of these 2MASS sources, and, for the flagged bright objects, we report only the  $grz$ -band MAG\_AUTO magnitudes and associated colors in the released catalogs.

After flagging saturated sources, comparison of the  $i$ -band magnitudes computed using SLR-derived colors in combination with either absolute  $r$ - and  $z$ -band magnitudes showed good agreement: 0.02 mag root-mean-square (rms) in the difference. Therefore, for simplicity, we set the zeropoints of all the bands using the  $r$ -band zeropoint calibration and the

SLR-derived colors. In Figure 4, we show an example of the SLR calibration for a typical BCS tile.

### 2.5. Photometry Validation

We perform several tests to check the accuracy of the photometric calibration. First, we compare photometry for objects in the few arc minute overlapping regions between neighboring tiles. As mentioned above, as each tile is calibrated independently and the edge regions are not included in the determination of the calibration solution, we can use these regions to test the quality of our photometric solutions. We note that, as this test is performed on the edges of the image where corrections for flat fielding are generally the poorest, the photometry in the central portion of the tile is potentially better. We report statistics for the median magnitude or color difference of objects in tiles for which this overlap region has  $\geq 100$  sources with signal to noise  $\geq 4$  in the  $r$ ,  $i$ , and  $z$  bands (204/233 tiles) or  $\geq 75$  sources in the  $g$  band (188/233 tiles). The results are shown in Figure 5. We divide the standard deviation measured from these distributions by  $\sqrt{2}$  to obtain the uncertainty on the calibration for a single tile. From these tests we measure 2.4% rms variation in  $i$ -band zeropoints. Checks on the colors show 1.9%, 1.3%, and 1.3% rms in the  $g - r$ ,  $r - i$ , and  $i - z$  calibration, respectively. Investigation of the

<sup>16</sup> We note these sources did not exceed the SATURATE keyword in the images' fits headers and so were not masked earlier in the reduction process.

<sup>17</sup> <https://www.astromatic.net/pubsvn/software/swarp/trunk/doc/swarp.pdf>

tile pairs with outlying median-color differences shows that the outliers predominately correspond to tiles with poorer seeing or significantly shallower-than-average data at the tile edges.

As another test, we use the stellar locus to check whether our reported magnitude uncertainties accurately reflect the measurement uncertainty. Using high signal-to-noise stars from the “high-quality” sample described in Covey et al. (2007) we identify low-scatter regions of the stellar locus that are locally linear in various color–color combinations. We then fit for these linear relations. For each tile in the BCS we test the reported uncertainties using these same color combinations. For each color–color pair we use stars where uncertainties in the abscissa color are small but errors in the ordinate color are greater than the locus scatter. This requirement ensures that the measured spread in the distribution around the above-described linear relation is dominated by our measurement uncertainty. To check the  $i - z$  color uncertainties we use stars with  $g - r < 1.2$ , for the  $g - r$  color we use  $0.5 < i - z < 0.8$  and for  $r - z$  we use stars with  $0.2 < g - i < 1.8$ . This test proved extremely useful—results on preliminary catalogs uncovered a small error in the coaddition process and identified single-epoch images to exclude from the coadds. The final distributions are well behaved, with some excess scatter again observed in filters with poorer seeing (this particularly affects the  $g$  band, as this band typically had worse seeing and lower sky noise).

### 2.6. Star–Galaxy Separation

Having created calibrated source catalogs, we now wish to cleanly divide them into samples of stars and galaxies. Cutting on the SExtractor star–galaxy statistic CLASS\_STAR is one way to define this division, however, examination of the resultant catalogs reveals non-negligible leakage of true galaxies into the stellar sample, even at high values of CLASS\_STAR.<sup>18</sup> In this section we introduce a new star–galaxy classification statistic, SG, and, using ground- and space-based imaging data, quantify the effectiveness of this statistic for star–galaxy separation.

To motivate this new statistic, consider an idealized scenario where stars are represented as two-dimensional Gaussian functions and galaxies have significantly more extended profiles; the sources have magnitude  $M_0$  as measured from a detection image. We can square this detection image and perform photometry at the locations of the previously identified sources to obtain a new “magnitude,”  $M_{SQ}$ . For the (Gaussian) stars, there is a trivial linear relation between  $M_0$  and  $M_{SQ}$ . Subtracting off this relation from the magnitude difference ( $M_0 - M_{SQ}$ ) of all sources sets the adjusted magnitude difference of the stellar population to zero while the galaxies, with considerably more extended profiles, cleanly form a separate population.

We use this approach to classify sources in the BCS data as follows. For each tile, we square the  $i$ -band detection images, source extract in dual image mode using the original  $i$ -band image as the detection image and then compute the difference in magnitudes between sources in the original and squared image. We fit a linear relation between  $M_0 - M_{SQ}$  and  $M_0$  for a clean stellar sample (here we use bright sources with  $i < 19.5$  and CLASS\_STAR  $\geq 0.98$ ) and subtract this relation from the magnitude differences to determine the adjusted magnitude difference  $\Delta$ :

$$\Delta = M_0 - M_{SQ} - (A_S M_0 + B_S) \quad (1)$$

<sup>18</sup> We note that the SLR algorithm employed in the previous section is fairly robust to this leakage (High et al. 2009), and we find no evidence the leakage is biasing our photometric calibration.

where  $A_S$  and  $B_S$  are the coefficients of the linear fit. The result of this process on a single tile is shown in the top left panel of Figure 6. As can be seen, the sources divide into two populations—with  $\Delta$  of stars centered around zero—until noise and limited resolution conspire to wash out morphological information. We find the separation between the two populations extends to fainter magnitudes using aperture photometry instead of MAG\_AUTO, so we calculate the difference using 3'' aperture magnitudes.

We next wish to probabilistically classify each source as a “star” or “galaxy.” We model the distribution of  $\Delta$ s for each of these populations as a Gaussian function and define the new star–galaxy statistic, SG, as the probability of a source being a star given both its  $\Delta$  value and a double Gaussian model fit to the data:

$$SG = \frac{A_{\text{star}} e^{\frac{(\Delta - \mu_{\text{star}})^2}{2\sigma_{\text{star}}^2}}}{A_{\text{star}} e^{\frac{(\Delta - \mu_{\text{star}})^2}{2\sigma_{\text{star}}^2}} + A_{\text{galaxy}} e^{\frac{(\Delta - \mu_{\text{galaxy}})^2}{2\sigma_{\text{galaxy}}^2}}} \quad (2)$$

where the parameters  $A$ ,  $\mu$ , and  $\sigma$  correspond to the amplitudes, means and standard deviations of the Gaussians derived from fits to the data, and—as with CLASS\_STAR—a value of 1 corresponds to a high probability of the source being a star. To allow for evolution in the  $\Delta$  parameter with magnitude, we fit the model to the sources in sets of 400 ordered by increasing magnitude. As there are few stars brighter than  $i = 19.5$  and we find CLASS\_STAR to be robust at this bright magnitude in all tiles, we use the CLASS\_STAR statistic for these sources. Finally, for the few sources with  $\Delta < 0$  and SG  $< 0.8$  we set SG to 2.0 as visual inspection of these objects indicates they are predominately image artifacts. In the top-right panel of Figure 6 we plot the distribution of SG versus source magnitude that results from the mapping of  $\Delta$  to SG by this process.

As for any morphological classifier, the magnitude limit to which this classifier is robust is highly seeing and depth dependent. This issue is clearly shown in the top left panel in Figure 6 where the  $\Delta$  values of the two populations overlap at faint magnitudes. Therefore, for each BCS tile, we conservatively record the new SG statistic up to the magnitude at which there are 9× as many stars as galaxies at the mean  $\Delta$  value,  $\mu_{\text{star}}$ , of the stellar population (i.e., 90% stellar purity at  $\Delta = \mu_{\text{star}}$ ) and report this limit as a column in Table 3. We include the  $\Delta$  values for all sources in the released catalogs to enable more aggressive faint source classification.

To quantify the performance of the new star–galaxy statistic, we use external optical- and spaced-based imaging from the Extended Groth strip. Using the same SExtractor settings as in the BCS, sources are extracted from deep, “best-seeing” (0''.65 FWHM)  $i$ -band coadds from the Canada–France–Hawaii Telescope Legacy Survey (Gwyn 2012). Owing to the excellent seeing in these coadds, we compute the SG statistic using 1''.5 aperture magnitudes to better demonstrate the power of this statistic as a morphological classifier (while the 3'' aperture-derived statistic proved robust in this test, the limiting magnitude was roughly 0.75 mag shallower as the larger aperture did not fully leverage the available spatial resolution). Using a 1'' association radius, we match this source list with the Advanced Camera for Surveys General Catalog (Griffith et al. 2012) which contains morphological information derived from HST imaging. Guided by Gray et al. (2009), we adopt an HST-based morphological classification using the SExtractor MAG\_BEST and FLUX\_RADIUS ( $r_{\text{flux}}$ ) parameters derived

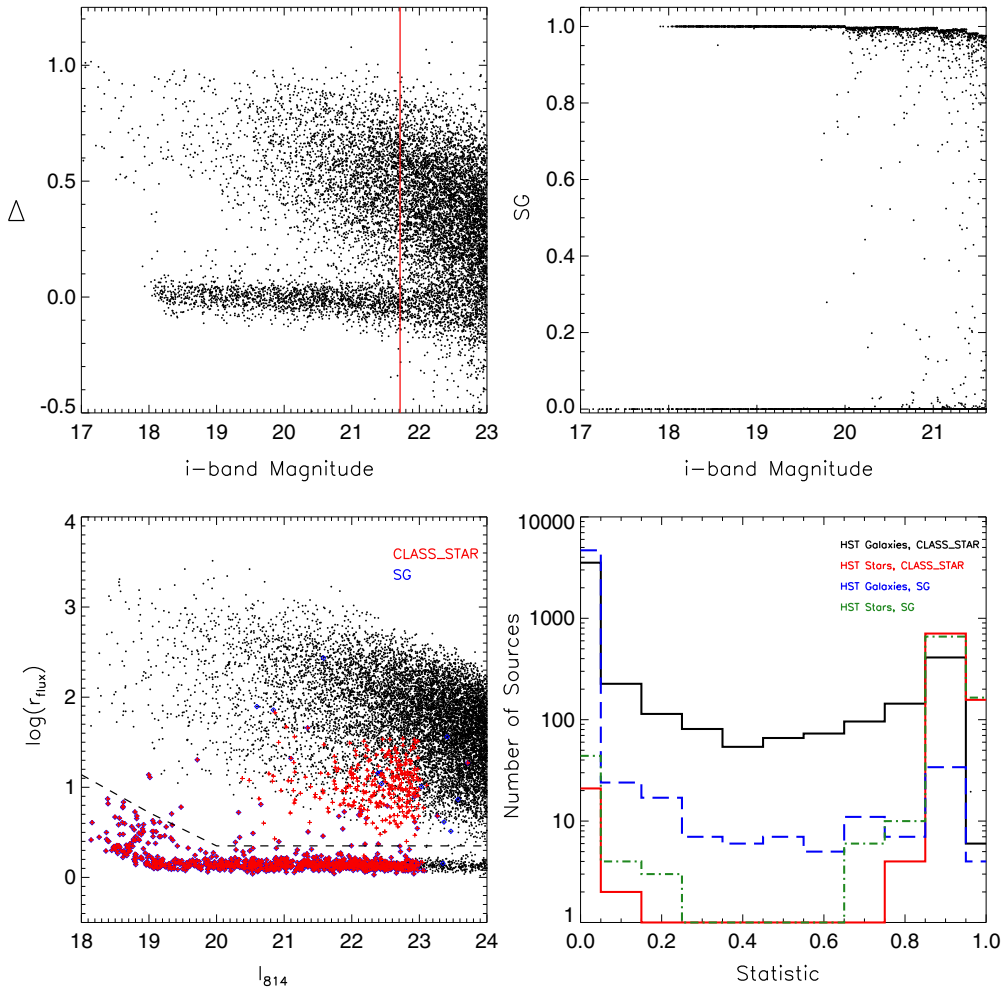


**Figure 6.** Top left: example of the new star–galaxy separation process discussed in Section 2.6 as applied to BCS tile 0511–5448. Plotted is the morphological parameter,  $\Delta$ , vs. magnitude; the stellar population forms a narrow band centered around 0. The solid red line corresponds to the *i*-band magnitude (21.7 for this tile) at which there is a ratio of 9 stars to each galaxy (90% stellar-purity) at the center of this band. Top right: the resulting distribution of SG values vs. *i*-band magnitude after star–galaxy classification for sources in shown in the previous panel with *i*-band magnitude brighter than 21.7. Bottom left: test of the new star–galaxy statistic using *HST*-classified sources in the Extended Groth strip. We classify sources below the black dashed-line in the  $I_{814}$ – $\log(r_{\text{flux}})$  plane as stars in the *HST* catalog. Overplotted in red are sources with  $\text{CLASS\_STAR} \geq 0.95$  and in blue are sources with  $\text{SG} \geq 0.8$ . The limiting classification magnitude (in the *i* band from the ground-based optical data) is determined as in the above panel. Bottom right: distribution of  $\text{CLASS\_STAR}$  and  $\text{SG}$  parameters for *HST*-classified galaxies (solid black and dashed-blue, respectively) and *HST*-classified stars (solid red and dot-dashed green). The last two panels demonstrate that significantly fewer galaxies are erroneously removed from a galaxy catalog generated from a cut on the star–galaxy statistic using  $\text{SG}$  compared to  $\text{CLASS\_STAR}$ .

**Table 3**  
Summary Information for BCS Data Presented in This Work

ID and Coordinates:			Seeing (arcsec)				$5\sigma$ Point Source Depth				Star Limit	Comments
BCS ID	R.A.	Decl.	<i>g</i>	<i>r</i>	<i>i</i>	<i>z</i>	<i>g</i>	<i>r</i>	<i>i</i>	<i>z</i>		
BCS0506–5601	76.708	−56.015	1.33	1.23	1.11	0.99	24.19	23.88	23.35	21.65	21.78	...
BCS0507–5412	76.985	−54.199	0.91	1.01	0.75	0.68	24.35	24.47	23.89	22.34	22.21	L, H
BCS0507–5448	76.897	−54.803	0.95	0.92	0.78	0.76	24.38	24.30	23.80	22.26	22.23	L, H
BCS0507–5524	76.804	−55.411	1.07	1.10	0.90	0.96	24.28	24.24	23.60	22.05	22.24	L, H
BCS0508–5223	77.195	−52.398	1.10	0.93	0.91	0.89	24.17	24.10	23.97	22.37	22.09	L, H
BCS0508–5300	77.174	−52.995	1.12	1.10	0.88	0.79	23.89	24.15	23.78	22.20	22.02	L, H
BCS0508–5336	77.067	−53.597	0.88	0.98	0.91	0.82	24.15	24.19	23.69	22.13	21.98	L, H
BCS0509–4959	77.482	−49.977	1.46	1.49	0.83	0.76	24.27	23.95	23.94	22.32	21.71	L, H
BCS0509–5035	77.414	−50.594	1.07	1.01	1.40	1.27	23.84	23.61	23.03	21.76	21.17	...
BCS0509–5111	77.345	−51.188	0.86	0.75	0.89	0.99	24.24	24.31	23.69	21.98	21.98	L, H

**Notes.** Summary information for the BCS imaging data presented in this work. Coordinate positions are given for the center of the  $36' \times 36'$  tiles. The reported seeing is the average FWHM of the seeing disk of the single epoch images that contribute to the coadded images. The point source depths are calculated as in Section 2.3 and the Star Limit corresponds to the faintest *i*-band magnitude for which we find robust morphological separation of stars and galaxies as described in Section 2.6. In the “Comments” field, “L” corresponds to tiles utilized in the low-redshift cluster search while “H” denotes tiles searched for higher-redshift systems (see Section 3).

(This table is available in its entirety in machine-readable form.)

**Table 4**  
Description of Catalog Columns

Column	Unit	Description
FIELDNAME	...	BCS tile name
OBJ_ID	...	Object Identification Number (unique per tile)
R.A.	degree	Right Ascension (J2000)
Decl.	degree	Declination (J2000)
G	AB Magnitude	<i>g</i> -band MAG_AUTO
GERR	AB Magnitude	<i>g</i> -band corrected magnitude uncertainty (See Section 2.3)
G_SEX	...	<i>g</i> -band Source Extractor Flags + Bright Star proximity flag <sup>a</sup>
G_CLASSSTAR	...	<i>g</i> -band Source Extractor Class Star
R	AB Magnitude	<i>r</i> -band MAG_AUTO
RERR	AB Magnitude	<i>r</i> -band corrected magnitude uncertainty (See Section 2.3)
R_SEX	...	<i>r</i> -band Source Extractor Flags + Bright star proximity flag <sup>a</sup>
R_CLASSSTAR	...	<i>r</i> -band Source Extractor Class Star
I	AB Magnitude	<i>i</i> -band MAG_AUTO
IERR	AB Magnitude	<i>i</i> -band corrected magnitude uncertainty (See Section 2.3)
I_SEX	...	<i>i</i> -band Source Extractor Flags + Bright star proximity flag <sup>a</sup>
I_CLASSSTAR	...	<i>i</i> -band Source Extractor Class Star
Z	AB Magnitude	<i>z</i> -band MAG_AUTO
ZERR	AB Magnitude	<i>z</i> -band corrected magnitude uncertainty (See Section 2.3)
Z_SEX	...	<i>z</i> -band Source Extractor Flags + Bright star proximity flag <sup>a</sup>
Z_CLASSSTAR	...	<i>z</i> -band Source Extractor Class Star
JTMASS	Vega Magnitude	2MASS <i>J</i> -band
JTMASS_ERR	Vega Magnitude	2MASS <i>J</i> -band uncertainty
GAUTO_ERR	AB Magnitude	Uncorrected <i>g</i> -band MAG_AUTO Uncertainty
RAUTO_ERR	AB Magnitude	Uncorrected <i>r</i> -band MAG_AUTO Uncertainty
IAUTO_ERR	AB Magnitude	Uncorrected <i>i</i> -band MAG_AUTO Uncertainty
ZAUTO_ERR	AB Magnitude	Uncorrected <i>z</i> -band MAG_AUTO Uncertainty
X_IMAGE	pixel units	Horizontal source location on tile
Y_IMAGE	pixel units	Vertical source location on tile
UNIFORM	...	Binary Flag, set to 1 if source is in nominal uniform-coverage region for the tile (See Section 2.3)
G4	AB Magnitude	Aperture-corrected 4'' <i>g</i> -band magnitude
R4	AB Magnitude	Aperture-corrected 4'' <i>r</i> -band magnitude
I4	AB Magnitude	Aperture-corrected 4'' <i>i</i> -band magnitude
Z4	AB Magnitude	Aperture-corrected 4'' <i>z</i> -band magnitude
G4_ERR	AB Magnitude	Aperture-corrected 4'' <i>g</i> -band magnitude uncertainty
R4_ERR	AB Magnitude	Aperture-corrected 4'' <i>r</i> -band magnitude uncertainty
I4_ERR	AB Magnitude	Aperture-corrected 4'' <i>i</i> -band magnitude uncertainty
Z4_ERR	AB Magnitude	Aperture-corrected 4'' <i>z</i> -band magnitude uncertainty
SG	...	New star-galaxy classification statistic (See Section 2.6)
DELTA_SQ	...	New star-galaxy statistic (See Section 2.6)

**Notes.** <sup>a</sup> Reported flags are the sum of all possible extraction flags (as is standard in SExtractor output). 0–124 Standard SExtractor flags 256 Missing data 512 Corrupted *i*-band (i.e., bright source that saturated in the *i* band, but not the *r* or *z* band) 1024 Photometry potentially corrupted owing to proximity to bright star.

from the  $I_{814}$  band. We classify as stars sources with  $i < 23$  (the SG-magnitude limit determined as described above) and

$$\log(r_{\text{flux}}) < \max(0.35, 1.50 - 0.05(I_{814} + 1), 8.7 - 0.42I_{814}).$$

The resulting  $\sim 900$  sources matching these criterion (out of  $\sim 5000$  total sources brighter than the magnitude cut) are used as the “true” stars in our evaluation of the ground-based morphological classifiers.

We plot comparisons of the CLASS\_STAR- and SG-classifications to the *HST* results in the bottom panels of Figure 6. As demonstrated in these panels, the SG-statistic shows significantly fewer galaxies misclassified as stars. For example, considering only sources brighter than the classification magnitude ( $i \leq 23$ ), a catalog generated from  $\text{SG} < 0.8$  contains 99% of all galaxies and removes 93% of all stars, while a similar catalog from  $\text{CLASS\_STAR} < 0.95$  includes 94% of all possible galaxies and excludes 95% of all stars.

### 3. CLUSTER EXTRACTION

Having created calibrated source catalogs, we now seek to identify clusters of galaxies in these data. There are three key ingredients for our cluster search, namely:

1. source catalogs from regions within the BCS survey that are of sufficient depth and uniformity for the cluster search;
2. a model for the colors and magnitudes of red-sequence cluster galaxies as a function of redshift;
3. the red-sequence cluster-finding algorithm.

We detail each of these components in this section.

#### 3.1. Search Area

As the BCS survey data is of heterogeneous depth and image quality (see, e.g., Figure 3), with substantial tile-to-tile (and within tiles, filter-to-filter) variation in both seeing and depth, it is necessary to identify subregions of the survey that are both sufficiently large and uniform as to allow the clean identification

of galaxy clusters. For our cluster search, we focus on the data in the  $r$ ,  $i$ ,  $z$  bands. We broadly divide the survey data into four categories.

1. *Poor quality tiles.* The data is either shallow in at least one of the filters of interest ( $i$ -band  $5\sigma$  point source depth  $m_i < 22$  or the typical  $i = 20.25$  galaxy has signal to noise less than 6 in the  $r - z$  color), observed in poor conditions ( $i$ - or  $r$ -band seeing in excess of  $1.^{\circ}6$ ) or is in a tile with prominent Galactic cirrus (BCS0532–5412, BCS0532–5448, BCS0536–5448, BCS0536–5412, BCS0540–5412, and BCS0540–5524). This data, 16% of the survey area, is not used in the cluster search.
2. *Acceptable tiles.* These tiles, the complement of the poor quality tiles, encompass 84% of the survey area.
3. *Fair quality tiles.* A deeper subset of the acceptable tiles where the typical signal to noise on the  $r - z$  color for a  $i = 22.75$  galaxy is between 2.5 and 3. This subset includes  $\sim 25\%$  of the acceptable data.
4. *Good quality tiles.* A still deeper subset of the acceptable tiles where the typical signal to noise on the  $r - z$  color for a  $i = 22.75$  galaxy is greater than 3. This subset includes  $\sim 50\%$  of the acceptable data.

As described below, we search the “acceptable” tiles for clusters at  $0.2 \leq z \leq 0.5$  and extend the cluster search in the two deeper regions to  $z \leq 0.75$ . We have chosen the upper redshift bounds of the cluster search in each region to ensure roughly uniform completeness of a typical  $m_{\star} + 1.5$  mag galaxy in  $i$  band at the highest redshift of interest (where here  $m_{\star}$  is the apparent magnitude of an  $M_{\star}$  galaxy; we describe our model below) and we only include those sources with  $i$ -band signal to noise greater than three and  $r$ -,  $z$ -band signal to noise greater than two in the cluster search. We flag the tiles searched for clusters in Table 3.

After identifying the data for the cluster search, we use the new statistic SG, to separate stars and galaxies for sources brighter than  $i = 20.5$  (corresponding to  $m_{\star}$  at  $z = 0.55$ ), classifying and excluding sources as stars when  $SG \geq 0.8$ , and retain all sources fainter than this limit. We choose this conservative magnitude for separation to mitigate spatial variations in source density induced by seeing variations in the stellar-excised source catalogs but revisit the problem of stellar contamination in Section 4.4. As the fields are at different galactic latitudes (and so have different levels of stellar contamination in the source catalog; see Section 4.4), we search each field independently for clusters.

### 3.2. Red-sequence Model

We create our model for the colors and magnitudes of red-sequence cluster galaxies as a function of redshift using the GALAXEV routines provided by Bruzual & Charlot (2003). The model galaxies are composed of passively evolving single stellar populations formed from an instantaneous star burst at redshift  $z = 3$ ; the stellar populations are drawn from the Salpeter initial mass function (Salpeter 1955) and follow the Padova 1994 evolutionary tracks (Fagotto et al. 1994). Metallicities are chosen based on analytical fits to RCS2 cluster data and cubic splines are used to interpolate the discrete output of the code to arbitrary redshifts. We anchor our model for  $m^*(z)$  to the low-redshift ( $0.05 < z < 0.35$ ) Rykoff et al. (2012) model for the maxBCG cluster sample by correcting our model for a small ( $\sim 0.2$  mag) offset between the models.

Using 47 clusters with spectroscopic redshifts ( $0.05 < z < 0.9$ ) selected from the SPT-SZ survey (Reichardt et al. 2013; Ruel et al. 2013) and processed in a similar fashion to the BCS survey data, we calibrate three red-sequence color–magnitude relations as a function of redshift:  $g - r$  versus  $i$ ,  $r - i$  versus  $i$ , and  $r - z$  versus  $i$ . This calibration is accomplished as follows.

First, for each cluster we identify an excess of galaxies in color–magnitude space around the SPT position. We then compare the colors and magnitudes of these galaxies with our red-sequence model to estimate the cluster redshift. To avoid the redshift determination being influenced by outliers or dominated by a few galaxies with small photometric uncertainties we bootstrap resample the galaxies and clip those with colors further than three sigma from the median offset from the red-sequence color–magnitude relation under consideration. For each bootstrap, the estimated redshift is the redshift at which the  $\chi^2$  statistic,

$$\chi^2 = \sum_{\text{galaxies}} \frac{[\text{Model(magnitude, color, } z) - \mathbf{g}]^2}{\text{color error}^2 + \sigma_{\text{rs}}^2}, \quad (3)$$

is minimized. Here  $\mathbf{g}$  encodes the color and magnitude of the galaxies, and  $\sigma_{\text{rs}} = 0.05$  (Koester et al. 2007b; Mei et al. 2009) is the intrinsic spread of the red sequence. We report the redshift as the median redshift of 100 bootstrap resamples.

We find a simple linear mapping of model redshifts  $z_{\text{model}}$  to spectroscopic redshifts,  $z_{\text{spec}}$ ,

$$z_{\text{spec}} = Az_{\text{model}} + B$$

is sufficient for tuning the  $g - r$  versus  $i$  red-sequence relation over the redshift range  $0.05 \leq z \leq 0.35$ . However, when extending the redshift range to  $z = 0.75$  ( $r - i$  versus  $i$ ) and  $z = 0.9$  ( $r - z$  versus  $i$ ), large structured residuals are apparent in the differences between the spectroscopic redshifts and the linearly corrected model redshifts. To better calibrate these color–magnitude relations, we instead adopt a non-linear mapping. As we do not, a priori, have a model for how to map the raw-model redshifts into the measured spectroscopic redshifts (only the expectation that such a mapping should be smoothly varying and monotonic), we use non-linear least squares minimization to fit the  $z_{\text{model}}$  and  $z_{\text{spec}}$  relation to a monotonic function generated using the methodology of Ramsay (1998) where we have chosen sines and cosines as the basis functions and include these functions to the fourth order.

We estimate the uncertainty in our model calibration by determining the quantity  $\delta z$  such that the reduced chi-squared statistic,  $\chi^2_{\text{red}}$ :

$$\chi^2_{\text{red}} = \frac{1}{v} \sum \frac{(z_{\text{estimated}} - z_{\text{spec}})^2}{(\delta z(1+z))^2} = 1,$$

where  $z_{\text{estimated}}$  is our calibrated model redshift and  $v$  is the number of degrees of freedom. Here the total degrees of freedom are reduced by 2 by the linear fit in the  $g - r$  versus  $i$  calibration and by 10 for the  $r - i$  versus  $i$  and  $r - z$  versus  $i$  calibration. We find uncertainties of  $\delta_z/(1+z) \sim 0.015\text{--}0.018$  for all of the redshift models. In Figure 7, we plot the results of our model calibration.

### 3.3. The Cluster-finding Algorithm

We detect clusters using an algorithm based on the cluster red-sequence (CRS) algorithm presented in Gladders & Yee (2000,

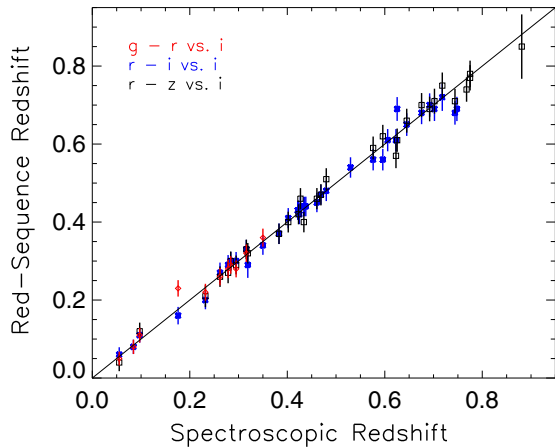


**Figure 7.** Results of red-sequence model training with a sample of spectroscopic clusters from the SPT-SZ survey. Plotted is the estimated vs. spectroscopic redshift for the  $g - r$  versus  $i$  band (red diamonds),  $r - i$  versus  $i$  band (blue crosses), and  $r - z$  versus  $i$  band (black boxes). The typical scatter, accounting for the degrees of freedom removed by the model fitting, is  $\delta_z/(1+z) \sim 0.018$ .

2005, hereafter GY00, GY05). The algorithm identifies clusters as over-densities of galaxies in position, color and magnitude space. Here we provide a brief overview of the algorithm and note key differences in our implementation as compared to the literature.

The CRS algorithm essentially converts a galaxy catalog into a three-dimensional datacube with axes (R.A., decl.,  $z$ ) whose voxels record the significance (positive or negative) of the red-sequence over-density at that location. Clusters are identified at voxel locations where the significance exceeds a fixed threshold (e.g.,  $\sigma \geq 3.29$  in GY05). Each redshift slice of our data cube is constructed as follows. To identify red-sequence over-densities in a redshift slice  $z = z_0$ , every galaxy in the catalog is first assigned a weight,  $W_g$ . This weight is based on two factors.

1. The consistency of the galaxy’s color (either  $g - r$  or  $r - z$ ) with that of a red-sequence galaxy at  $z = z_0$  with identical  $i$ -band magnitude.
2. The  $i$ -band magnitude of the galaxy. We construct this weighting as in GY00 but, to sample similar galaxy populations at low- and high- $z$ , set  $W_g = 0$  for galaxies with  $m \geq m_{\star}(z_0) + 1.5$ .

The weighted galaxies are then binned into  $0.25'$  cells and, as in GY00, the resulting weighted density map is smoothed with a kernel

$$k(r) = Ae^{-1.965r/r_c}. \quad (4)$$

We set  $r_c = 350$  kpc; we explored a variety of  $r_c$  values (ranging from 250 to 450 kpc) and found the results to be relatively independent of the scale.

To assess the relative rarity of the density values in the map, we create “random” realizations by bootstrap resampling the galaxies that contribute non-zero weight to the density map. One hundred such realizations are created for each redshift slice and we use the distribution values from these realizations to create a mapping from density to the standard normal distribution. We use this mapping to assign each pixel in our redshift slice a Gaussian significance.

This process is then repeated to create significance maps at a series of redshift slices with spacing  $\delta z = 0.02$ ; these slices are then combined to create the three-dimensional datacube. We identify clusters at voxel locations that exceed a significance

threshold of  $3.1\sigma$  and where at least five galaxies have contributed any weight to the detection (the additional constraint is necessary to reduce spurious detections at high redshift). This threshold, determined using mock catalogs (described in Section 5), was chosen to limit catalog impurity (including the failure mode of selecting small clumps of large clusters as separate systems) while maximizing completeness.

### 3.4. Application to the BCS Data

The largest change in our implementation of the CRS algorithm from GY00 and GY05 lies in the procedure for combining the small  $0.33 \text{ deg}^2$  tiles into larger blocks for the cluster search and background estimation. Given the heterogeneity of the BCS survey, it is impossible to apply the rigorous image matching technique of GY05 and still obtain blocks of sufficiently large area for robust background estimation. Instead, we simplify the problem by restricting our cluster search to lower redshifts and brighter magnitudes where the differences in photometric errors between tiles are reduced; this simplification motivated the survey divisions described in Section 3.1.

We identify roughly uniform coverage areas for background estimation using the weight maps produced by SWarp for each tile during the coaddition process: we mark as “good” the  $0.3'$  pixels that have greater than one-third of the median weight, lie inside the nominal central region of the tile, and are not in a region previously flagged during the cataloging process (see Section 2.3). We next rebin these small pixels into the  $0.25'$  pixels that are used by the cluster detection algorithm and mask the  $0.25'$  pixels for which less than 75% of the pixel area is marked for inclusion. Density values are drawn from unmasked pixels during the bootstrap resampling step. We include the edge regions of the tiles in the cluster search as they provide a natural taper at the edge of each tile but exclude them from the bootstrapping process as the coverage at the tile edges is significantly more variable than in the central regions. As a consequence, clusters on tile edges have reduced detectability and we flag the systems that are identified in these edge regions in the final cluster catalog.

For each field we conduct a series of cluster searches that we ultimately combine to construct our final cluster catalog. First, we conduct two searches for clusters at relatively low redshifts in the “acceptable” quality tiles: we use the  $g$ -,  $r$ -,  $i$ -band data to detect clusters at redshifts  $0.15 < z < 0.35$  and we then extend the search to redshift  $z = 0.5$  using the  $r$ -,  $i$ -,  $z$ -band data. We then use the “fair” and “good” quality tiles to identify clusters out to  $z = 0.75$  using the  $r$ -,  $i$ -,  $z$ -band data. We have slightly overlapped the redshift ranges of the searches in these data sets to avoid missing clusters at the redshift boundaries. As an illustration of the cluster-detection process, a redshift slice from the low-redshift search of the 23<sup>h</sup> field and a pair of clusters identified by the algorithm is shown in Figure 8.

## 4. CLUSTER CHARACTERIZATION

Following the initial cluster extraction we determine several properties for each cluster: its redshift, brightest cluster galaxy (BCG), and optical richness. In this section we detail the determination of each of these quantities.

### 4.1. Redshift Remeasurement

We first remeasure the redshift of each cluster. To determine the redshift we select all galaxies that contribute to the cluster detection and then compute the cluster redshift as described in

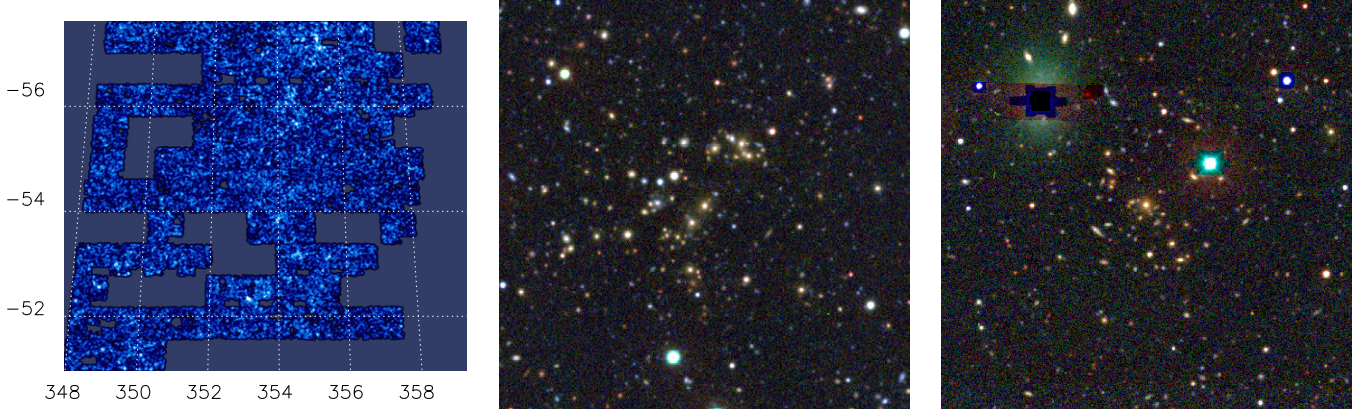


**Figure 8.** Left: example red-sequence significance map at  $z = 0.47$  from the low- $z$  cluster search in the  $23^h$  field. Poor quality tiles, masked stars and bad amplifiers create the holes in the map. The color scale ranges from  $-2.5$  to  $3.3\sigma$ . Middle: LCS-CLJ231509-5233.6 (SCSO-J231511-523322), a rich cluster from this redshift slice at  $z = 0.47$  with richness,  $\lambda(0.4 L_*) = 27$ . Right: a more typical cluster, LCS-CLJ233818-5238.1, at  $z = 0.54$  and richness  $\lambda(0.4 L_*) = 10.5$  identified in a higher- $z$  search.

Section 3.2. We use the average of  $r - i$  versus  $i$  and  $r - z$  versus  $i$  red-sequence redshifts to determine the redshift for all systems. When this estimated redshift is below  $z = 0.35$  we further refine the estimate using the  $g - r$  versus  $i$  red-sequence model. The redshift uncertainty is reported as the rms of 100 bootstrap-estimated redshifts added in quadrature with a minimum scatter determined during both our spectroscopic tuning and catalog merging process (see below) of  $\delta_z/(1+z) = 0.02$ . In general we find good agreement with the initial redshift estimate from the cluster finder itself except at the boundaries of the searched redshift-range, or, for systems selected during of the  $g - r$  versus  $i$  cluster search, where initial redshifts were mis-estimated owing to color-redshift degeneracies.

#### 4.2. BCG Selection

Following measurement of the cluster redshift, we next determine the BCG of each system. For the BCG we pick the brightest galaxy within a box in the  $r - z$  color,  $i$ -band magnitude plane such that

1. its  $i$ -band magnitude falls in the range:  $m_* - 3 < i < m_*$ ;
2. its  $r - z$  color is within than  $3.5\sigma$  of the red-sequence model at the cluster redshift; and
3. the galaxy is located within 350 kpc of the cluster-finder determined location.

If no such galaxy exists, we expand the search radius to 450 kpc. If no galaxy is found in this expanded search, we report the cluster location at the position returned by the cluster-finder and flag the system, otherwise we report the BCG position as the location of the cluster. After this automated selection we visually inspect all BCGs and manually select an alternative BCG for  $\sim 30$  systems where the BCG was misidentified owing to artifacts, deblending issues in the cluster core or was not included in the catalog owing the presence of bright stars.

The search radius was chosen based on a coarse optimization in simulations as well as visual inspection of the selected centers in  $rgb$  image cutouts around the clusters. We chose a fixed radius independent of cluster size as, while 350 kpc is a large fraction of  $r_{500}$  for smaller clusters, the searched area is small enough that there are few bright galaxies to misidentify as the BCG. This selection may be too simplistic; further data is required to test the fidelity of our centering algorithm.

#### 4.3. Richness

After BCG selection we determine the optical richness of each cluster. For our richness measure we use  $\lambda$ , a statistic optimized to minimize the scatter in the mass-richness relation (Rykoff et al. 2012). Much like the red-sequence cluster finder developed in GY00, the  $\lambda$  statistic includes spatial, magnitude and color weighting to optimize the contrast of cluster galaxies against the background (Rozo et al. 2009; Rykoff et al. 2012).

To compute  $\lambda$  we modify the code provided for the SDSS data set by Rykoff et al. (2012)<sup>19</sup> to utilize our red-sequence model and measurements of the background source density in color-magnitude space. We estimate two backgrounds for the BCS, one for each field, as the fields are centered at different galactic latitudes ( $b = -33^\circ$  for the  $5^h$  field and  $b = -58^\circ$  for the  $23^h$  field) and our star-galaxy separation does not extend to the faint limits of the BCS catalogs. We report  $\lambda$  using the  $r - i$  versus  $i$  red-sequence relation as this color-magnitude combination has the smallest photometric errors in the BCS. For each cluster, we use the best-fit  $r - i$  versus  $i$  red-sequence model, but enforce  $L_*$  limits using the best-fit redshifts as determined above. Simple Monte Carlo tests, as well as tests with mock catalogs, show that for BCS-depth data accurate richnesses can be determined out to redshift  $z = 0.75$  counting galaxies to  $0.4 L_*$  and to  $z = 0.55$  counting to  $0.2 L_*$ . As the  $i$ -band data is significantly deeper than the other bands for red-sequence objects, the relatively larger photometric uncertainties in the  $r$  band determine these limits rather than incompleteness in the catalogs.

After the  $\lambda$  computation, we merge the catalogs from the low- and high- $z$  cluster searches. For every candidate we search for other candidates within the aperture determined by the  $\lambda$  algorithm (see Equation (4) of Rykoff et al. 2012), and within  $\delta z = 0.05$  in redshift. For all matched pairs of candidates we robustly estimate the scatter in the redshift differences between the pairs, finding a spread of  $\delta_z/(1+z) = 0.011$  in the difference. As many of the member galaxies are in common, we consider this extra scatter to be added by the cluster-finding process and so add it in quadrature with the model uncertainty determined during the spectroscopic tuning process. This produces a floor

<sup>19</sup> <http://kipac.stanford.edu/maxbcg/lambdarichness.pro>

in the redshift uncertainty of  $\delta_z/(1+z) = 0.02$ .<sup>20</sup> We next match clusters within the richness aperture and  $3\sigma$  of the redshift scatter from the matched pairs. As this merger procedure is designed to both merge separate cluster catalogs and to remove sub-clumps of rich clusters from the final catalog, we select the richer of the two systems when duplicates occur. Finally, we visually inspect the  $\sim 20$  clusters with potential counterparts within  $1'$  but outside the redshift cut. We exclude the few systems which are clearly composed of a small subset of galaxies from a richer lower-redshift system or are clearly mis-measured at the boundary redshift of the low- $z$  search.

#### 4.4. Stellar Contamination of the Cluster Catalog

With the fairly conservative bright star cut at  $i = 20.5$ , the excision of stars from the source catalogs used for the cluster search is not complete. While the ratio of stars to galaxies falls at fainter magnitudes, the presence of stars (especially class-M stars which have similar colors and magnitudes as high-redshift cluster galaxies) can add scatter to richness estimates and, because of the steeply rising number counts of clusters with decreasing richness, can artificially boost the number of systems above a fixed richness threshold. We explore the effect of stellar contamination using the 90% (96%) of the tiles searched for clusters (high- $z$  clusters) for which the star–galaxy separation is robust to  $i = 21.5$ ; this deeper cut is sufficient to excise stars to  $m_* + 1.0$  at  $z = 0.55$  compared to  $z = 0.38$  for the conservative cut. We test for the contamination separately in the  $23^h$  and  $5^h$  fields as we expect any effects to be more pronounced in the lower galactic latitude  $5^h$  field.

Comparing the numbers of clusters at  $\lambda(0.4 L_*) > 10$  and  $0.55 < z < 0.75$  in the  $5^h$  field we find 272 systems in the deeper star-cut catalogs opposed to 282 in the shallow (5% decrease). Similarly in the  $23^h$  field we find 135/138 clusters in the shallower/deeper-cut catalogs (2% decrease). While some differences in richness may be caused by the removal of actual cluster galaxies with this stricter cut (as we are probing the faint limit of the star–galaxy separation), our tests in the Extended Groth Strip (Section 2.6) show that this leakage should be small. As the star–galaxy separation effects a declining fraction of the source population as the redshift increases, (i.e., with a fixed magnitude limit we can excise stars to a magnitude comparable to an  $m_* + 1$  galaxy at  $z = 0.55$  but only to  $\sim m_*$  at  $z = 0.75$ ), this test places a lower limit on the number of poor groups boosted above our richness threshold. In light of these results, we estimate  $\lambda$  with the deeper stellar-excised catalogs where possible.

#### 4.5. Compensating for Masked Regions

As a last step, we compensate for the systematic reduction in richness owing to masked regions around the cluster. These masks were created using the weight maps produced by SWarp for each tile during the coaddition process: we mark as “good” the  $0.^{\prime}3$  pixels that have greater than one-third of the median weight and are not in a region previously flagged during the cataloging process (see Section 2.3). Using these masks, we compute and apply this richness correction as follows.

First, for every cluster we compute the fraction of area masked around the BCG in 100 kpc-wide rings out to a radius of

2 Mpc. Using the galaxy weights provided by the  $\lambda$ -algorithm we then compute an area-corrected richness-per-radial bin for each cluster. We then combine data from clusters from both fields (to improve statistics) to measure the “average” richness-per-radial bin as a function of richness. We use clusters at redshifts between  $0.3 < z < 0.75$  to calculate the average for  $\lambda(0.4 L_*)$ -richness and  $0.3 < z < 0.55$  for  $\lambda(0.2 L_*)$ . This average is derived from hundreds of systems at the low-richness down to  $\sim 10$  clusters for the richest systems.

Based on the masking around each individual cluster we then compute a correction to its richness. If this richness correction pushes the system into a higher-richness bin, we iterate the correction process until the correction converges. We report the corrected richnesses as well as the value of the richness-correction as entries in the cluster tables.

## 5. TESTS ON SIMULATED CATALOGS

We characterize the efficacy of our cluster finder using simulated catalogs. In this section we describe the simulated catalogs, our application of the cluster finder to these simulations, and our characterization of the completeness and purity of the resulting cluster catalogs. We consider these results to be an idealized test of the cluster finder as we have not incorporated various non-idealities of real observations (e.g., variations in depth, masked regions) in the mock catalogs.

The mock galaxy sample is drawn from a  $220 \text{ deg}^2$  lightcone populated with galaxies down to a flux limit  $i \sim 25$  in the redshift range  $0 < z < 1.3$ . The underlying dark matter distribution is based on a cosmological simulation of  $1 h^{-1} \text{ Gpc}$ ; this simulation is a single “Carmen” simulation from the Large Suite of Dark Matter Simulations<sup>21</sup> project (McBride et al. 2011). The lightcone was created by pasting together 34 separate snapshots. The Adding Density Determined Galaxies to Lightcone Simulations (ADDGALS) algorithm is then run to assign galaxies to the dark matter particles in a way that reproduces the known luminosities and two-point function. Using a training set of low-redshift spectroscopic galaxies from SDSS DR5, spectral energy distributions are then assigned to the galaxies in such a way as to reproduce the observed magnitude–color–environment relations. These simulated catalogs produce realistic distributions of galaxies and their colors, including a well defined cluster red sequence. Because of these properties, the catalogs have previously been used for tests of cluster finding (Koester et al. 2007b; Hao et al. 2010; Soares-Santos et al. 2011; Rykoff et al. 2014), photometric redshifts (Gerdes et al. 2010), and spectroscopic followup strategies (Cunha et al. 2012). The technique was previously presented in Wechsler (2004), Busha & Wechsler (2008), and a full description of the algorithm and the simulated sky catalogs it produces will be presented in R. H. Wechsler et al. (in preparation) and M. T. Busha et al. (in preparation). In addition to these galaxy catalogs, the simulations also include the locations and masses,  $M_{200}$ , for  $\sim 220,000$  dark matter halos with  $M_{200} > 5 \times 10^{12}$ . As we seek to use galaxy groups and clusters as tracers of massive dark matter halos, we will use these halo catalogs to assess the purity and completeness of our cluster sample.

We degrade the mock catalogs to match the typical depth of the BCS data by adding to the model galaxy fluxes a random deviate drawn from the normal distribution,  $N(0, \sigma_{\text{BCS}})$ :

$$\text{Flux} = \text{Flux}_{\text{true}} + N(0, \sigma_{\text{BCS}}). \quad (5)$$

<sup>20</sup> We find similar scatter in the mock catalogs (Section 5), where the initial tuning with 30 rich systems showed a scatter of  $\delta_z/(1+z) = 0.007$  and the final catalog showed a net scatter of  $\delta_z/(1+z) = 0.014$  around the true redshifts, an extra scatter of  $0.012 \times (1+z)$ .

<sup>21</sup> <http://lss.phy.vanderbilt.edu/lasdamas>

Here  $\sigma_{\text{BCS}}$  is the typical source flux uncertainty in each band:  $\sigma_{\text{BCS}} = 0.19, 0.21, 0.35$ , and  $1.3 \mu\text{Jy}$  in the  $g$ ,  $r$ ,  $i$ , and  $z$  bands, respectively. The fluxes are converted to magnitudes and sources with  $i$ -band signal to noise less than three or  $r$ -,  $z$ -band signal to noise less than two are excluded; we do not attempt to include the effects of incompleteness beyond these signal-to-noise constraints. We split the simulated catalog into ten patches of  $22 \text{ deg}^2$  each, roughly the size of each tile-grouping used in the BCS cluster-search.

We next tune our synthetic red-sequence models to match the simulated data. This tuning proceeds analogously to the procedure described in Section 3.2 except, in the place of the massive SPT clusters, we select 30 halos from the simulations with redshift,  $z_h$ ,  $0.09 < z_h < 0.9$  and  $M_{200} > 3 \times 10^{14} M_\odot$ . We identify an excess of red-sequence galaxies around these systems and determine a monotonic mapping of our synthetic model redshifts to the simulation redshifts.

We then run the cluster-finding algorithm on these simulated catalogs and compare the resultant cluster catalog with the dark matter halo catalog to assess both the purity and completeness of the cluster sample. Here we define the “purity” of the catalog as the fraction of clusters which have a halo counterpart with  $M_{200} > 2 \times 10^{13}$  and the “completeness” of the cluster sample at a fixed mass threshold,  $M_t$ , as the fraction of dark matter halos with  $M_{200} \geq M_t$  that have a counterpart in our cluster sample. We identify dark matter halo counterparts for our clusters using similar criteria to Dong et al. (2008): a cluster is determined to be associated with a halo if the projected distance between the cluster and halo center is less than  $r_{200}$  and the redshift difference is  $|\delta z| < 0.035 \times (1 + z_h)$  (i.e.,  $2.5 \times$  the typical scatter of recovered redshifts of  $\delta_z/(1 + z) = 0.014$ ).

It is necessary to define various cuts when constructing a cluster sample and we use the simulations to guide our choice of these cuts. The values of the cuts, here on both the cluster detection significance and the cluster richness, are a trade-off between sample purity and sample completeness (e.g., by lowering the significance threshold we can boost the completeness of the sample at the expense of more spurious detections; however this decline in purity can be offset by requiring a higher richness threshold). Using results from simulations to iterate on our choice of cuts, we find that requiring detection significance  $> 3.1$  and  $\lambda(0.4 L_\star) > 10$  strikes a good balance in creating a sample with high purity and completeness. As the photometric uncertainties in the BCS preclude accurate richness measurements above  $z = 0.75$ , we truncate our catalog at this redshift and reserve further exploration of the cluster-finder at higher redshifts for future work.

We demonstrate the results of our cluster finder on these simulated catalogs in Figure 9: when adopting the matching criteria discussed above the sample the measured purity of the sample exceeds 85%. Expanding the redshift scaling to  $|\delta z| < 0.05 \times (1 + z_h)$  to account for redshift outliers, the purity exceeds 90%. The completeness of the sample is plotted in the bottom-left panel and is  $\sim 80\%$  for clusters at  $M_{200} \gtrsim 1 \times 10^{14} M_\odot$ .

We next assess whether our algorithm successfully recovers the “true”-richness,  $\lambda_{\text{true}}$ , of the halos. For each halo, this quantity is computed using the noiseless mock magnitudes and the richness aperture is centered on the galaxy marked as the BCG of the halo. For the majority of clusters, we find good agreement between our recovered richness,  $\lambda_{\text{recovered}}$ , and  $\lambda_{\text{true}}$  (median difference  $\Delta\lambda = 0.5$ ,  $\sigma_{\Delta\lambda} = 3$ , with the richness measurements recovered from the degraded simulation

data being lower than the true values). We have tracked the galaxies contributing to each cluster detection as well as their true host halos and find that the outliers are primarily driven by false associations between clusters and halos or (for a small number of cases) the wrong choice of cluster BCG. Considering only those halos richer than our catalog threshold ( $\lambda_{\text{true}} > 10$ ; bottom-right panel of Figure 9), the completeness is 90% at  $M_{200} \gtrsim 1 \times 10^{14} M_\odot$ . Exploring the missing halos above this mass we find 75% of the missing systems exceed our cluster extraction threshold in the cluster-finder datacube. As such, these systems are either falling outside our redshift search, below the richness threshold or being merged with a nearby system. We have explored this completeness for the  $\lambda_{\text{true}} > 10$  halos both above and below the median BCS sample redshift ( $z = 0.52$ ) and find that, for the simulated data, our upper redshift limit is sufficiently conservative that our completeness is roughly independent of redshift.

## 6. THE CLUSTER CATALOG

The final cluster catalog extracted from the BCS consists of 764 clusters at  $z \leq 0.75$  with  $\lambda(0.4 L_\star) \geq 10$ ; more than 85% of the sample is newly discovered. The median redshift of the sample is  $z = 0.52$  and the median richness is  $\lambda(0.4 L_\star) = 16.4$ . The redshift and richness distributions of the catalog are plotted in Figure 10. We denote these systems by the acronym “LCS,” for Little Cluster Survey, in light of the ongoing Dark Energy Survey<sup>22</sup> which is in the midst of a 5 yr survey that will image  $5000 \text{ deg}^2$  of the southern sky, including the BCS region. In Tables 5 and 6 we report the locations, redshifts, and richnesses of the systems as well as previous identifications in the literature. This search for counterparts in the literature was conducted by querying the SIMBAD<sup>23</sup> database and searching for previously-identified clusters within  $3'$  of each system. In the remainder of this section, we conduct a more detailed comparison of our cluster selection to that of other samples of clusters within the BCS footprint.

### 6.1. Comparisons to Other Cluster Catalogs

There are only a small number of surveys with significant numbers of clusters in the BCS footprint: the Southern Cosmology Survey (SCS; Menanteau et al. 2009, 2010), the XMM-BCS survey (Šuhada et al. 2012), and the SPT and ACT mm-wave surveys (Vanderlinde et al. 2010; Reichardt et al. 2013; Marriage et al. 2011). Here, we only compare our sample to clusters identified in these surveys if they fall within the redshift range searched for a given BCS tile—e.g., we do not consider a high- $z$  system to be “missed” in our cluster search if the cluster-finding algorithm was not run at high redshifts. Taking into account possible differences in redshift-estimation accuracy we use cuts of  $0.15 < z < 0.55$  for tiles used in the low-redshift cluster search and extend the upper redshift bound to  $z = 0.9$  for regions included in the higher-redshift search. We consider clusters to be a “match” if they are within  $|\delta z| < 0.2$  and within the richness algorithm cutoff radius (typically 900 kpc). We adopt the large redshift matching-criterion to avoid missing systems due to differences in estimated redshifts (in particular, we find large discrepancies between our redshifts and the redshifts reported in Menanteau et al. (2010) for the SCS systems, similar to those reported in Šuhada et al. (2012)). As expanded on

<sup>22</sup> [www.darkenergysurvey.org](http://www.darkenergysurvey.org)

<sup>23</sup> <http://simbad.u-strasbg.fr/simbad>

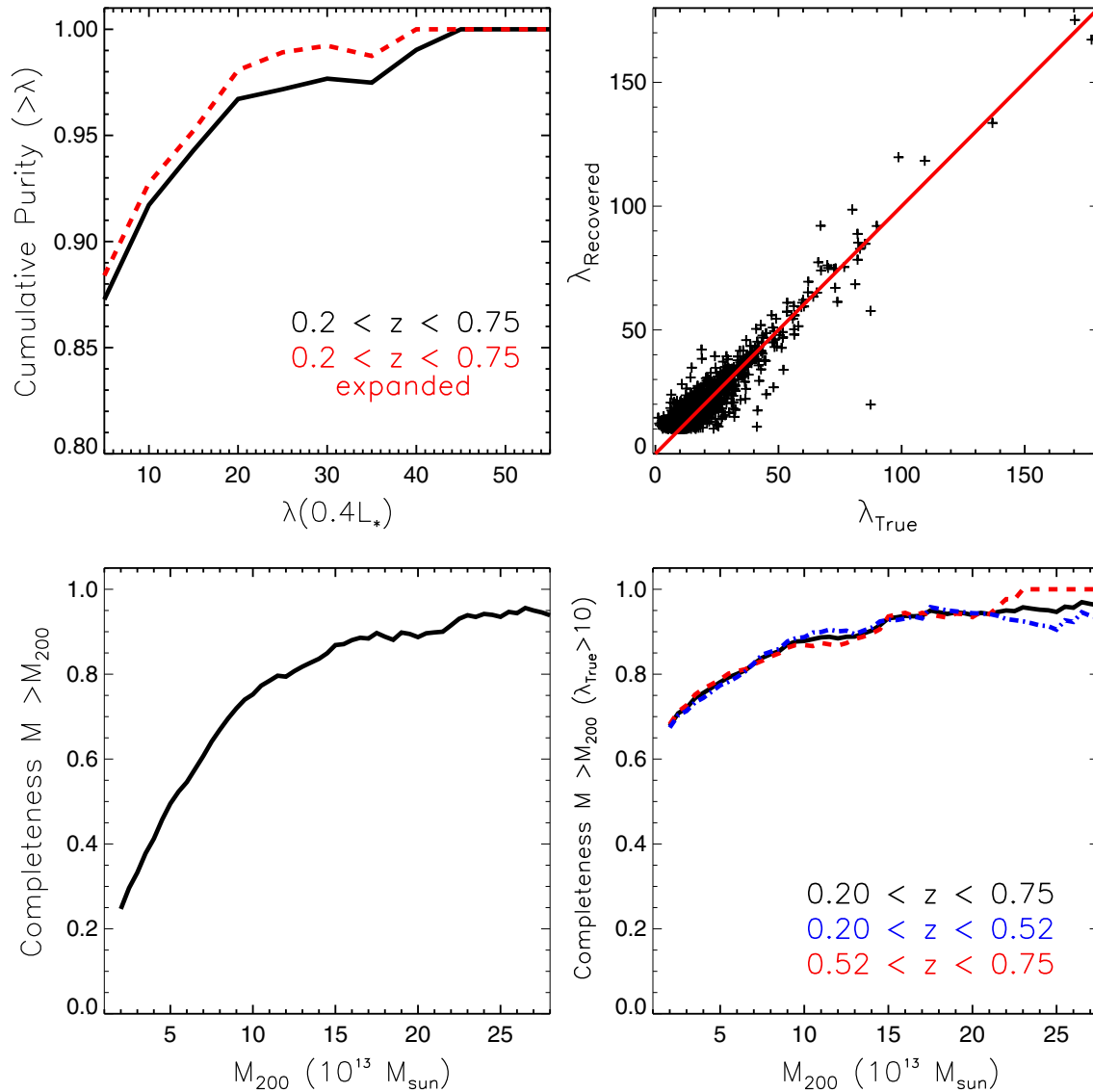


**Figure 9.** Purity and completeness tests of the cluster-detection algorithm on mock catalogs (Section 5). Top left: fraction of clusters at  $0.2 < z < 0.75$  matched to dark matter halos with  $M_{200} > 2 \times 10^{13} M_{\odot}$ . We consider a cluster to be associated with a halo if it is within  $r_{200}$  and the difference between the cluster and halo redshift is  $|\Delta z| < 0.035 \times (1 + z_h)$ . Expanding the redshift matching criterion to  $|\Delta z| < 0.05 \times (1 + z_{\text{halo}})$  (red-dashed line) captures redshift outliers and marginally increases the purity. Top right:  $\lambda_{\text{true}}$  vs. measured  $\lambda$  for matched halo-cluster matches at  $z < 0.75$ ; over-plotted in red is the 1-1 relation. Outliers in this plot are primarily caused by false associations between the halo and cluster or the wrong choice of BCG. Bottom left: cumulative completeness for  $M > M_{200}$  of the cluster catalog. The cluster sample is 80% complete for clusters at  $M_{200} \gtrsim 1 \times 10^{14} M_{\odot}$ . Bottom right: cumulative completeness of the cluster catalog only considering halos with  $\lambda_{\text{true}} > 10$ . We have explored this completeness both above and below the median BCS sample redshift ( $z = 0.52$ ) and find that our upper redshift limit is sufficiently conservative that our completeness is roughly independent of redshift.

below, the results proceed as expected: we recover the majority of the optically selected clusters from SCS catalog, a significant fraction of the XMM-BCS catalog with the non-recovered systems generally residing at lower masses, and all of the massive systems from the SZ-surveys that lie in non-masked regions.

The SCS cluster sample, an optically selected sample drawn from an alternative reduction of the BCS, provides the largest catalog of clusters for comparison: 65 systems lie within the redshift range and footprint searched. These systems were selected based on their galaxy content to have masses  $M_{200} > 3 \times 10^{14} M_{\odot}$  (where the mass here is defined with respect to the mean density of the universe (Menanteau et al. 2010)). Of these 65 clusters, 54 have counterparts in our catalogs. Of the remaining 11 systems, four are matched by clusters detected by our cluster-finder but at richnesses below our cutoff threshold, two were significantly masked within  $1'$  around the SCS-BCG

by our automated masking procedure, for two clusters both algorithms identified the same cluster but selected significantly-separated BCGs, one cluster was not detected in our search and the remaining two SCS-detected clusters were not found as their redshifts (as measured by our algorithm) lie outside of the range searched. Inverting the question, for tiles the catalogs share in common and using  $\lambda(0.4L_*)$  as the richness metric, we find SCS counterparts for 20/25 (32/50) of the richest systems in these regions.

From the XMM-BCS catalog there are 40 systems in this comparison (we include the “lower-quality” detections in this check). As is typical for a flux-limited X-ray survey, the XMM-BCS systems span a broad range in mass, with a median mass of  $M_{500} \approx 1 \times 10^{14} M_{\odot}$  as derived from the X-ray luminosities (Šuhada et al. 2012). Of the 40 clusters, 23 of the systems have counterparts in our catalog while an additional seven were

**Table 5**  
Optically Selected Galaxy Clusters Located in the 23 h BCS field

ID	R.A.	Decl.	z	$\delta z$	Sigma	$\lambda$	$\delta\lambda$	$\Delta\lambda$	$\lambda(0.2 L_*)$	$\delta\lambda(0.2 L_*)$	$\Delta\lambda(0.2 L_*)$	Mask 200 kpc	Mask 500 kpc	Edge of Tile	Previous ID
LCS-CL J231218–5109.2	348.0766	−51.1548	0.32	0.025	3.21	14.4	2	1.3	23.8	3	2.6	0.00	0.05	1	...
LCS-CL J231224–5115.3	348.1009	−51.2560	0.75	0.040	3.27	14.0	3	0.0	...	...	...	0.00	0.01	...	...
LCS-CL J231230–5214.0	348.1262	−52.2335	0.28	0.024	4.14	14.1	2	1.3	18.3	3	1.9	0.00	0.03	1	...
LCS-CL J231235–5218.6	348.1469	−52.3114	0.42	0.031	4.11	16.3	2	0.9	34.0	4	2.2	0.00	0.03	...	...
LCS-CL J231240–5201.3	348.1674	−52.0220	0.49	0.033	3.65	11.7	2	0.4	17.2	3	0.6	0.00	0.04	...	...
LCS-CL J231253–5203.4	348.2222	−52.0570	0.69	0.040	3.51	12.1	2	0.1	...	...	...	0.00	0.00	...	...
LCS-CL J231305–5259.0	348.2729	−52.9843	0.65	0.037	3.93	11.0	2	0.5	...	...	...	0.01	0.01	...	...
LCS-CL J231309–5101.5	348.2886	−51.0254	0.33	0.024	4.67	21.0	2	1.1	37.1	4	2.7	0.04	0.03	...	...
LCS-CL J231313–5405.1	348.3052	−54.0859	0.20	0.021	3.43	13.0	2	1.5	17.0	3	2.1	0.16	0.05	1	...
LCS-CL J231321–5435.2	348.3404	−54.5878	0.56	0.035	3.37	14.2	3	4.3	...	...	...	0.28	0.32	1	...

**Notes.** Galaxy Clusters selected above  $3.1\sigma$  with  $\lambda(0.4 L_*)$  greater than 10 and  $z \leq 0.75$  in the 23<sup>h</sup> field. We report the cluster ID, the BCG position, red-sequence redshift and uncertainty and detection significance. For richnesses derived to  $0.4 L_*$  and  $0.2 L_*$  (for  $z < 0.55$ ) we include the optical richness ( $\lambda$ ), richness uncertainty and the amount the richness was boosted to account for masking. Additionally, we report the fraction of area masked within 200 and 500 kpc, flag the system if it is located on the edge of a tile, and note if the cluster has a previous identification. The reported richness uncertainty is the uncertainty estimate from the richness algorithm (see Equation (3) of Rykoff et al. 2012) added in quadrature with a Poisson uncertainty from masked-area compensation. The previous identification column designates a counterpart using the criterion of Section 6. Tags correspond to the following works: 0 ACO (Abell et al. 1989) 1 REFLEX (Böhringer et al. 2004), 2 Southern Cosmology Survey (Menanteau et al. 2009, 2010), 3 SPT-SZ Survey (Vanderlinde et al. 2010; Reichardt et al. 2013), 4 ACT (Marriage et al. 2011), 5 XMM-BCS (Šuhada et al. 2012), 6 PLANCK (Planck Collaboration et al. 2014) 7 Vikhlinin et al. (1998) 8 Buckley-Geer et al. (2011).

(This table is available in its entirety in machine-readable form.)

**Table 6**  
Optically Selected Galaxy Clusters Located in the 5 h BCS field

ID	R.A.	Decl.	z	$\delta z$	Sigma	$\lambda$	$\delta\lambda$	$\Delta\lambda$	$\lambda(0.2 L_*)$	$\delta\lambda(0.2 L_*)$	$\Delta\lambda(0.2 L_*)$	Mask 200 kpc	Mask 500 kpc	Edge of Tile	Previous ID
LCS-CL J050624–5423.5	76.6001	−54.3925	0.50	0.033	4.56	11.8	2	0.5	12.9	2	0.5	0.00	0.03	...	...
LCS-CL J050715–5145.6	76.8148	−51.7607	0.64	0.037	3.63	14.5	3	2.4	...	...	...	0.00	0.10	1	...
LCS-CL J050728–5431.4	76.8682	−54.5246	0.45	0.033	3.64	11.1	2	1.9	17.8	3	3.0	0.31	0.17	1	...
LCS-CL J050735–5218.0	76.8994	−52.3001	0.43	0.031	4.84	11.2	2	0.5	19.5	3	1.0	0.00	0.05	...	...
LCS-CL J050736–5119.8	76.9020	−51.3314	0.62	0.040	3.39	17.8	3	2.1	...	...	...	0.00	0.01	1	...
LCS-CL J050805–5217.6	77.0214	−52.2947	0.61	0.036	3.66	12.1	2	0.7	...	...	...	0.00	0.06	...	...
LCS-CL J050806–5248.4	77.0285	−52.8081	0.69	0.039	3.66	23.8	3	0.6	...	...	...	0.02	0.00	...	...
LCS-CL J050813–5213.4	77.0571	−52.2241	0.39	0.035	3.58	11.8	2	1.6	11.5	2	1.5	0.17	0.09	...	...
LCS-CL J050818–5400.3	77.0770	−54.0063	0.74	0.039	3.45	18.7	3	0.2	...	...	...	0.00	0.00	...	...
LCS-CL J050820–5423.0	77.0873	−54.3848	0.60	0.037	3.94	12.7	2	0.3	...	...	...	0.00	0.03	...	...

**Notes.** The same as Table 5, except for clusters selected in the 5<sup>h</sup> field.

(This table is available in its entirety in machine-readable form.)

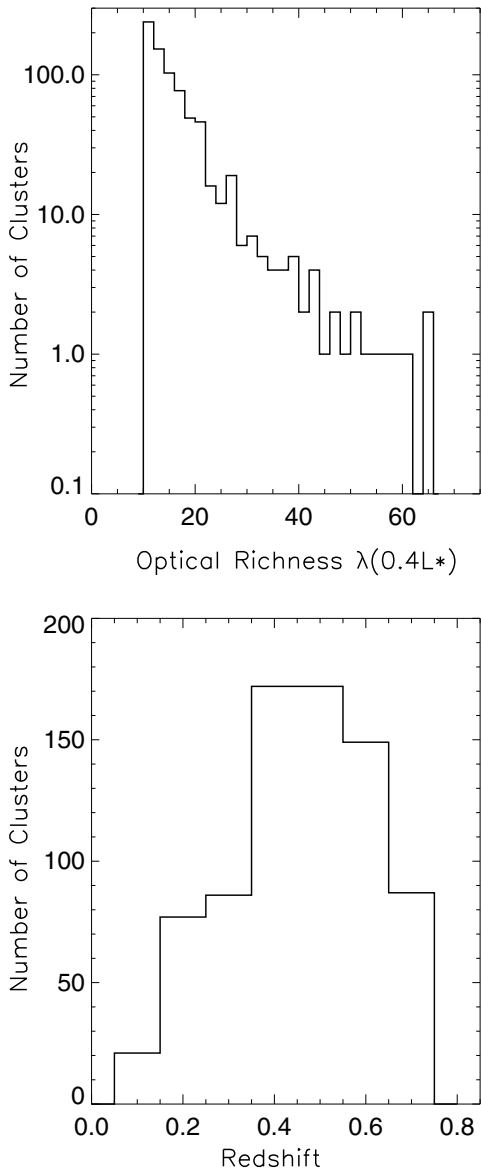


**Figure 10.** Top: distribution in optical richness,  $\lambda$ , measured to  $0.4 L_\star$  for the 764 clusters at  $z \leq 0.75$ . Bottom: redshift distribution of the full cluster catalog. This sample has a median redshift of  $z = 0.52$  and median optical richness of  $\lambda(0.4 L_\star) = 16.4$ .

detected by the cluster-finder but have richesses below the cutoff threshold. For the matched systems we find the redshifts to be on average consistent within the quoted uncertainties. The outstanding ten non-recovered systems have estimated masses ranging from  $M_{200} \sim 4-25 \times 10^{13} M_\odot$ . Three of these systems are termed “lower-quality” detections in the X-ray data (Šuhada et al. 2012) and have masses  $M_{200} < 1 \times 10^{14} M_\odot$  and five of these systems lie on the edges of BCS tiles where coverage is less uniform.

Finally, we consider the SZ-selected clusters. The clusters are massive, with  $M_{200} > 5.6 \times 10^{14} M_\odot$  (Reichardt et al. 2013; Marriage et al. 2011). Of the 10 possible systems, 8 have counterparts in our catalog while the remaining two non-recovered clusters have greater than 50% of the area within 1' of the reported center masked owing to the presence of bright stars. Not surprisingly (as some of these systems were used in our red-sequence model training), there is good agreement between our estimated redshifts and the literature redshifts for these systems.

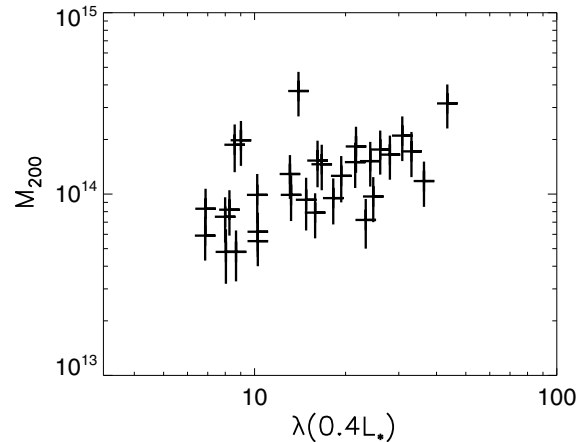


**Figure 11.** X-ray luminosity determined-mass vs. richness for 31 clusters from the XMM-BCS survey (Šuhada et al. 2012) with counterparts in the LCS cluster sample. Here we have relaxed the  $\lambda > 10$  criterion to increase the number of matches. There is a clear correlation between optical richness and mass; the three most significant outliers are found to either be in the uneven coverage regions at the edges of the BCS tiles or have centers significantly offset from the X-ray position. Both of these effects likely decrease the measured cluster richness.

## 6.2. Mass–Richness Relation

While calibrating the  $\lambda$ -mass relation is beyond the scope of this work, we briefly examine the issue using the XMM-BCS sample. In Figure 11, we plot the relation between richness and mass derived from X-ray luminosity for those XMM-BCS systems with counterparts in the LCS sample. Here we have relaxed the  $\lambda > 10$  criterion to increase the number of matches. There is a clear correlation between optical richness and mass; the most significant outliers from the general trend are found to either have BCGs significantly offset from the X-ray position or to fall in the uneven coverage regions at the edges of BCS tiles. Upcoming large and high- $z$  X-ray samples from e.g., the XXL survey<sup>24</sup>—the southern XXL field lies within the BCS 23<sup>h</sup> field—and *eRosita* (Cappelluti et al. 2011), will be powerful data sets with which to both quantify and improve the accuracy of our cluster centering algorithm and to calibrate the mass–richness relation for these systems.

## 7. SUMMARY AND FUTURE WORK

In this paper, we have presented our reductions of  $\sim 80$  deg<sup>2</sup> of optical imaging data from the Blanco Cosmology Survey and detailed the creation of calibrated source catalogs extracted from these data. We introduced a new, easily implemented morphological star–galaxy separation statistic, SG, and quantified the effectiveness of this statistic using external high-quality ground- and space-based data. Using a red-sequence-based cluster-finding algorithm, we have searched the BCS for galaxy clusters. We report the coordinates, redshifts, and optical richesses for 764 clusters at  $z \leq 0.75$ , of which greater than  $> 85\%$  are new detections. This sample has a median redshift of  $z = 0.52$  and median optical richness,  $\lambda$ , of  $\lambda(0.4 L_\star) = 16.4$ . Based on tests with realistic mock catalogs, the catalog is expected to have a purity in excess of 85% and to be  $> 80\%$  complete at  $M_{200} > 1 \times 10^{14} M_\odot$ . The creation of the cluster sample is intended as a first step toward a multi-wavelength study of optically selected clusters in the survey region.

Indeed, one of the greatest strengths of the Blanco Cosmology Survey is its overlap with a wide assortment of multi-wavelength

<sup>24</sup> <http://irfu.cea.fr/xxl/>

data. The optical source catalogs presented here have already been combined with mm-wave data from SPT to both confirm cluster candidates and estimate redshifts for SZ-selected clusters in the SPT-SZ survey (Reichardt et al. 2013; Song et al. 2012) and to make the first measurement of galaxy bias from the gravitational lensing of the Cosmic Microwave Background (Bleem et al. 2012). As others may find the data products described in this work useful, we are publicly releasing the reduced  $g$ -,  $r$ -,  $i$ -,  $z$ -band images, weight maps, and the calibrated source catalogs for this  $\sim 80$  deg $^2$  survey. These products are available at <http://data.rcc.uchicago.edu/dataset/blanco-cosmology-survey>.

The authors thank Michael Huff for assistance with flagging spurious objects in the source catalogs and Doug Rudd for his assistance setting up the online data access. L.B. thanks Tom Crawford for useful discussions. L.B. acknowledges support by the U.S. Department of Energy, Basic Energy Sciences, Office of Science, under Contract No. DE-AC02-06CH11357, the NSF Physics Frontier Center award PHY-0551142, and the NSF OPP award ANT-0638937. Galaxy cluster research at SAO is supported in part by NSF grants AST-1009649 and MRI-0723073. This research draws on data provided by NOAO PI 2005B-0043 as distributed by the NOAO Science Archive. NOAO is operated by the Association of Universities for Research in Astronomy (AURA), Inc. under a cooperative agreement with the National Science Foundation. Characterization of the new star–galaxy classifier was based on both data from both AEGIS (a multi-wavelength sky survey conducted with the *Chandra*, *GALEX*, *Hubble*, Keck, CFHT, MMT, Subaru, Palomar, *Spitzer*, VLA, and other telescopes and supported in part by the NSF, NASA, and the STFC) and on observations obtained with MegaPrime/MegaCam, a joint project of CFHT and CEA/DAPNIA, at the Canada–France–Hawaii Telescope (CFHT) which is operated by the National Research Council (NRC) of Canada, the Institut National des Sciences de l’Univers of the Centre National de la Recherche Scientifique (CNRS) of France, and the University of Hawaii. This work is based in part on data products produced at the Canadian Astronomy Data Centre as part of the Canada–France–Hawaii Telescope Legacy Survey, a collaborative project of NRC and CNRS. Additionally, this research has made use of the SIMBAD database, operated at CDS, Strasbourg, France. Finally, the authors acknowledge the University of Chicago Research Computing Center for hosting the data products presented in this work.

*Facility:* Blanco (MOSAIC II)

## APPENDIX

In this appendix, we provide a summary of the information for each BCS tile in Table 3. The format of the available source catalogs is available in Table 4. The locations, redshifts, and richnesses of galaxy clusters identified from these data are available in Tables 5 and 6. Images and calibrated catalogs are available at <http://data.rcc.uchicago.edu/dataset/blanco-cosmology-survey>.

## REFERENCES

- Abell, G. O. 1958, *ApJS*, 3, 211
- Abell, G. O., Corwin, H. G., Jr., & Olowin, R. P. 1989, *ApJS*, 70, 1
- Allen, S. W., Evrard, A. E., & Mantz, A. B. 2011, *ARA&A*, 49, 409
- Ashby, M. L. N., Stanford, S. A., Brodwin, M., et al. 2013, *ApJS*, 209, 22
- Ashby, M. L. N., Stern, D., Brodwin, M., et al. 2009, *ApJ*, 701, 428
- Austermann, J. E., Aird, K. A., Beall, J. A., et al. 2012, Proc. SPIE, 8452, 84521E
- Bertin, E., & Arnouts, S. 1996, *A&AS*, 117, 393
- Bertin, E., Mellier, Y., Radovich, M., et al. 2002, in ASP Conf. Ser. 281, Astronomical Data Analysis Software and Systems XI, ed. D. A. Bohlender, D. Durand, & T. H. Handley (San Francisco, CA: ASP), 228
- Bleem, L. E., van Engelen, A., Holder, G. P., et al. 2012, *ApJL*, 753, L9
- Böhringer, H., Schuecker, P., Guzzo, L., et al. 2004, *A&A*, 425, 367
- Brown, M. J. I., Dey, A., Jannuzzi, B. T., et al. 2007, *ApJ*, 654, 858
- Bruzual, G., & Charlot, S. 2003, *MNRAS*, 344, 1000
- Buckley-Geer, E. J., Lin, H., Drabek, E. R., et al. 2011, *ApJ*, 742, 48
- Busha, M. T., & Wechsler, R. H. 2008, in 43rd Rencontres de Moriond, Cosmology
- Cappelluti, N., Predehl, P., Böhringer, H., et al. 2011, *MSAIS*, 17, 159
- Carlstrom, J. E., Ade, P. A. R., Aird, K. A., et al. 2011, *PASP*, 123, 568
- Covey, K. R., Ivezić, Ž., Schlegel, D., et al. 2007, *AJ*, 134, 2398
- Cunha, C. 2009, *PhRvD*, 79, 063009
- Cunha, C. E., Huterer, D., Busha, M. T., & Wechsler, R. H. 2012, *MNRAS*, 423, 909
- Desai, S., Armstrong, R., Mohr, J. J., et al. 2012, *ApJ*, 757, 83
- Dong, F., Pierpaoli, E., Gunn, J. E., & Wechsler, R. H. 2008, *ApJ*, 676, 868
- Dünner, R., Hasselfield, M., Marriage, T. A., et al. 2013, *ApJ*, 762, 10
- Fagotto, F., Bressan, A., Bertelli, G., & Chiosi, C. 1994, *A&AS*, 104, 365
- Gerdes, D. W., Sypniewski, A. J., McKay, T. A., et al. 2010, *ApJ*, 715, 823
- Gilbank, D. G., Gladders, M. D., Yee, H. K. C., & Hsieh, B. C. 2011, *AJ*, 141, 94
- Gladders, M. D., & Yee, H. K. C. 2000, *AJ*, 120, 2148
- Gladders, M. D., & Yee, H. K. C. 2005, *ApJS*, 157, 1
- Gray, M. E., Wolf, C., Barden, M., et al. 2009, *MNRAS*, 393, 1275
- Griffith, R. L., Cooper, M. C., Newman, J. A., et al. 2012, *ApJS*, 200, 9
- Gwyn, S. D. J. 2012, *AJ*, 143, 38
- Hao, J., McKay, T. A., Koester, B. P., et al. 2010, *ApJS*, 191, 254
- High, F. W., Stalder, B., Song, J., et al. 2010, *ApJ*, 723, 1736
- High, F. W., Stubbs, C. W., Rest, A., Stalder, B., & Challis, P. 2009, *AJ*, 138, 110
- Holder, G. P., Viero, M. P., Zahn, O., et al. 2013, *ApJL*, 771, L16
- Ivezić, Ž., Smith, J. A., Miknaitis, G., et al. 2007, *AJ*, 134, 973
- Kaiser, N., Burgett, W., Chambers, K., et al. 2010, *Proc. SPIE*, 7733, 77330E
- Koester, B. P., McKay, T. A., Annis, J., et al. 2007a, *ApJ*, 660, 239
- Koester, B. P., McKay, T. A., Annis, J., et al. 2007b, *ApJ*, 660, 221
- Marriage, T. A., Acquaviva, V., Ade, P. A. R., et al. 2011, *ApJ*, 737, 61
- McBride, C., et al. 2011, *BAAS*, 43, 249.07
- Mei, S., Holden, B. P., Blakeslee, J. P., et al. 2009, *ApJ*, 690, 42
- Menanteau, F., Hughes, J. P., Barrientos, L. F., et al. 2010, *ApJS*, 191, 340
- Menanteau, F., Hughes, J. P., Jimenez, R., et al. 2009, *ApJ*, 698, 1221
- Miknaitis, G., Pignata, G., Rest, A., et al. 2007, *ApJ*, 666, 674
- Planck Collaboration, Ade, P. A. R., Aghanim, N., et al. 2014, *A&A*, 571, A29
- Planck Collaboration, Aghanim, N., Arnaud, M., Ashdown, M., et al. 2011, *A&A*, 536, A12
- Ramsay, J. O. 1998, J. R. Stat. Soc.: Ser. B (Stat. Methodol.), 60, 365
- Reichardt, C. L., Stalder, B., Bleem, L. E., et al. 2013, *ApJ*, 763, 127
- Rest, A., Stubbs, C., Becker, A. C., et al. 2005, *ApJ*, 634, 1103
- Rozo, E., Bartlett, J. G., Evrard, A. E., & Rykoff, E. S. 2014, *MNRAS*, 438, 78
- Rozo, E., Rykoff, E. S., Evrard, A., et al. 2009, *ApJ*, 699, 768
- Ruel, J., Bazin, G., Bayliss, M., et al. 2014, *ApJ*, 792, 45
- Rykoff, E. S., Koester, B. P., Rozo, E., et al. 2012, *ApJ*, 746, 178
- Rykoff, E. S., Rozo, E., Busha, M. T., et al. 2014, *ApJ*, 785, 104
- Salpeter, E. E. 1955, *ApJ*, 121, 161
- Sehgal, N., Addison, G., Battaglia, N., et al. 2013, *ApJ*, 767, 38
- Skrutskie, M. F., Cutri, R. M., Stiening, R., et al. 2006, *AJ*, 131, 1163
- Soares-Santos, M., de Carvalho, R. R., Annis, J., et al. 2011, *ApJ*, 727, 45
- Song, J., Zenteno, A., Stalder, B., et al. 2012, *ApJ*, 761, 22
- Sunyaev, R. A., & Zel’dovich, Y. B. 1972, *CoASP*, 4, 173
- Szabo, T., Pierpaoli, E., Dong, F., Pipino, A., & Gunn, J. 2011, *ApJ*, 736, 21
- Suhada, R., Song, J., Böhringer, H., et al. 2012, *A&A*, 537, A39
- Takada, M. 2010, in AIP Conf. Ser. 1279, Deciphering the Ancient Universe with Gamma-Ray Bursts, ed. N. Kawai & S. Nagataki (Melville, NY: AIP), 120
- Vanderlinde, K., Crawford, T. M., de Haan, T., et al. 2010, *ApJ*, 722, 1180
- Vikhlinin, A., McNamara, B. R., Forman, W., et al. 1998, *ApJ*, 502, 558
- Wechsler, R. H. 2004, in Clusters of Galaxies: Probes of Cosmological Structure and Galaxy Evolution, ed. J. S. Mulchaey, A. Dressler, & A. Oemler (Pasadena, CA: Carnegie Observatories), 53
- Wen, Z. L., Han, J. L., & Liu, F. S. 2009, *ApJS*, 183, 197
- Wen, Z. L., Han, J. L., & Liu, F. S. 2012, *ApJS*, 199, 34
- Wu, H.-Y., Rozo, E., & Wechsler, R. H. 2010, *ApJ*, 713, 1207
- York, D. G., Adelman, J., Anderson, J. E., Jr., et al. 2000, *AJ*, 120, 1579